Scaling of Point-Absorber Wave Energy Converter Hydrodynamics

Curtis J. Rusch

A dissertation
submitted in partial fulfillment of the
requirements for the degree of

Doctor of Philosophy

University of Washington

2021

Reading Committee:

Brian L. Polagye, Chair

Benjamin Maurer

Per Reinhall

Program Authorized to Offer Degree:
Mechanical Engineering

University of Washington

Abstract

Scaling of Point-Absorber Wave Energy Converter Hydrodynamics

Curtis J. Rusch

Chair of the Supervisory Committee:
Associate Professor Brian L. Polagye
Mechanical Engineering

Wave energy converters (WECs) are devices that generate mechanical or electrical power from the motion of ocean waves. Point absorber WECs react to the motion of the ocean waves at or near the surface, and have a characteristic surface expression of less than one tenth of a wavelength. Two-body, point absorber WECs rely on the reaction force produced by a submerged component, usually a heave plate, to capture power from ocean waves. This work is motivated by limited understanding of heave plate hydrodynamics, necessary to produce accurate WEC models.

In oscillatory flow, drag and inertial forces experienced by flat plates and cylinders have been shown to vary with the Keulegan-Carpenter number. We demonstrate that this extends to an asymmetric hexagonal conic heave plate suitable for a point absorber WEC. The forces on three geometric scales of this plate were measured by forced oscillation experiments in quiescent water. From these measurements, phase-invariant and phase-dependent coefficients of drag and added mass are calculated using a Morison decomposition. For low amplitude oscillations, the total force experienced by the conic heave plate is well-described by phase-invariant coefficients that scale with the Keulegan-Carpenter number. However, for larger oscillations, maximum forces are better described by phase-dependent coefficients. Flow visualization is used to interpret the phase variations.

We explore the role of heave plate topology on fluid reaction forces using three representative shapes: a hexagonal flat plate, a hexagonal conic with an open top, and the same with a closed top that encloses a fluid mass. We force each test article sinusoidally in a quiescent tank and decompose the reaction force using forms of the Morison equation for phase-invariant and phase-dependent parameterizations. We find that a flat plate generates 5.3% more fluid reaction force than the open conic topology, and 21.4% more than the enclosed conic. We also show that asymmetric topologies generate asymmetric reaction forces, but the magnitude of asymmetry is limited by nearly symmetric fluid inertia forces, which dominate over drag for these test articles. Additionally, we observe asymmetric vortex dynamics for the flat plate when the Keulegan-Carpenter number is between 1 and 2, accompanied by a shift in the phase of the peak force by $\approx 7\%$ of the oscillation period. As a consequence of this shift, the hydrodynamic coefficients estimated from the phase-dependent Morison equation decomposition are asymmetric, suggesting that phase-dependent representations may not provide physical insight in some hydrodynamic regimes and that flat plates may have multiple reaction force profiles for a range of Keulegan-Carpenter numbers.

Finally, we apply results from heave plate experiments to models of a two-body point absorber WEC. We approximate these hydrodynamics using three parameterizations: (1) as low-fidelity coefficients invariant across sea state, accurate only at the reference sea state, (2) mid-fidelity coefficients dependent on the oscillation amplitude, but invariant in phase, which accurately represent forces for small amplitude motions, and (3) high-fidelity coefficients dependent on both oscillation amplitude and phase, which represent hydrodynamic forces accurately for all oscillation amplitudes. As dynamical models of WECs often rely on a low-fidelity representation, it is important to understand how this practice impacts wave energy converter modelling and whether code bases should be extended to incorporate higher-fidelity representations of heave plate hydrodynamics. Here, we validate an analytical model for a two-body point absorber WEC against field data and a dynamical model. We then use the

analytical model to evaluate the effect of these parameterizations on estimates of heave plate motion, tension between the float and heave plate, and electrical power output from the WEC.

We find that predictions of electrical power output using mid-fidelity coefficients differ by up to 30% from models using low-fidelity coefficients for regular waves ranging in height from 0.5 - 1.9 m. High-fidelity coefficients, however, yield less than a 5% change when compared with mid-fidelity coefficients. This suggests that mid-fidelity coefficients can be important for accurate wave energy converter modeling, but the added complexity of high-fidelity coefficients yields little further benefit. We show similar, though less pronounced, trends in maximum tether tension, while heave plate motion has only a weak dependence on coefficient fidelity. Finally, we emphasize the importance of using experimentally derived added mass over that calculated from boundary element methods (another common practice for dynamical models), which can lead to substantial under-prediction of power output and peak tether tension.

In total, this work experimentally characterizes the hydrodynamics of asymmetric heave plates across scale and topology, touches on the intricacies of vortex behavior in these experiments, and models two-body WECs using heave plate hydrodynamic parmeterizations of varying fidelity to determine the impact on WEC behavior. This fills a gap in the literature in asymmetric heave plate hydrodynamics. This also provides the first characterization of the impact of enclosed fluid on the reaction force heave plates provide to point absorber WECs. Moreover, we provide guidance on the use of these hydrodynamic parameterizations to WEC modellers, assessing the changes seen in model behavior for low-, mid-, and high-fidelity hydrodynamic representations.

TABLE OF CONTENTS

LIST OF FIGURES

LIST OF TABLES

NOMENCLATURE

WEC	wave energy converter
KC	Keulegan-Carpenter number
C_d	coefficient of drag
C_a	coefficient of added mass
C_{fi}	coefficient of fluid inertia
g	gravity
ρ	fluid density
t	time
D	effective diameter
A	oscillation amplitude
H	oscillation height
T	oscillation period
θ	phase
z	vertical position
$\dot{z}$	vertical velocity
$\ddot{z}$	vertical acceleration
m_{hp}	heave plate mass

F_h hydrodynamic force

F_d drag force

F_a added mass force

F_i inertial force

$F_{i,\text{enclosed}}$ enclosed fluid inertia force

F_w weight

F_b buoyancy

F_{fluid} fluid force

$F_{measured}$ measured force

$\overline{F_h}$ hydrodynamic force reconstructed with phase-invariant coefficients

$\widetilde{F_h}$ hydrodynamic force reconstructed with phase-dependent coefficients

E_{re} peak reconstruction error

$F_{\text{fluid},va}$ vertical fluid force asymmetry

ACKNOWLEDGMENTS

I owe thanks to countless people for their support getting me to, and then through, graduate school. First, thank you to Brian Polagye, my advisor, for your guidance and belief in me throughout graduate school. I have greatly benefited from your support of a healthy work-life balance (even if you don't practice what you preach) and appreciated our 'running meetings', trips to Mazama, and skiing, hiking and climbing trips. You ask probing research questions and have helped mold me into a better scientist and engineer.

I also want to thank the rest of my committee for their help and guidance. Ben Maurer, you have been an incredible person to turn to for support - whether that was standing at your white board to scribble equations for an hour, watching you climb into my tank to retrieve a dropped piece of plexiglass, or staying on a zoom call extra long to talk things through with me, your kindness and intelligence has been inspiring. Tim Mundon, you have been a brilliant collaborator to work and chat with, and I am grateful for all your questions and experimental suggestions. I can't wait to see what Oscilla Power does next, and hope we can continue to find projects to work together on. Per Reinhall, thank you for joining my committee and taking the time to familiarize yourself with my work amid a transition from ME chair and across multiple time zones. Chris Chickadel, thank you for being ready and willing to step in as my GSR - being able to turn to you took a lot of stress off of my plate.

For the heave plate tests, there were many individuals that helped me along the way. Thank you to Adam Brown and Jim Thomson for laying the groundwork for dockside oscillator testing. Rob Cavagnaro, your work to develop the MATLAB control software made my tank experiments possible. Corey Crisp, thank you for your countless hours of help troubleshooting grounding issues and electrical noise. Ama Hartman, your machining skill,

outside the box thinking, and steady data analysis was crucial to the completion of heave plate topology testing. A big thank you to Andy Hamilton at MBARI for making the tank tests of the 1:1 scale plate happen, and for sitting with me all day while we collected data. The support of John Ferriera was also instrumental in the MBARI tests.

A large, multi-institutional team made possible the field testing of WEBS. Andy Stewart, thank you for putting your trust in me to both model and help deploy WEBS. The WEC itself could not have been built without Paul Gibbs, Jesse Dosher, Aaron Marburg, James Joslin, the APL machine shop, and all of the engineers at C-Power. Thanks to Andy Hamilton, John Ferriera, and François Cazenave at MBARI, the captain of the Shana Rae, Jim Christmann and all others involved in the WEBS project at UW-APL and MBARI for their contributions to field data. Additional thanks Zhe Zhang for assistance with troubleshooting models of WEBS.

Collaboration contributed greatly to my graduate experience, and though not all of the work ended up published, I learned a lot from so many star collaborators. Tim Mundon and Brian Rosenberg at Oscilla Power have been trustworthy collaborators and friends for the duration of my PhD, and I can't wait to continue finding projects that help us blur the lines between industry and academia. I appreciated working with CalWave on the heave plate geometry work, including Thomas Boerner, Nigel Kojimoto, Bryan Murray, Marcus Lehmann. The team at the West Coast Wave Initiative at the University of Victoria was instrumental in boosting my numerical modelling skills - special thanks to Helen Bailey and Bryson Robertson for teaching and hosting me for two weeks. Ryan Nicoll and the team at Dynamic Systems Analysis have provided top notch software support and even incorporated asymmetric drag into Proteus after I asked if it was possible. Christian Windt has been great to work with after approaching me following my 2019 EWTEC talk, and I look forward to seeing your career take off. Matt Leary and Bryson Robertson (since moving to Oregon State University), have been excellent modellers to work with. A big shout out to the students of

INORE for making the marine energy field feel so much more like a family.

To the students of MREL: James Joslin, Rob Cavagnaro, Trevor Harrison, Paul Murphy, Ben Strom, Hannah Ross, Dom Forbush, Emma Cotter, Corey Crisp, Jess Noe, Kate Van Ness, Trent Dillon, Isabel Scherl, Hannah Aaronson, Carl Stringer, Zach Tully, Aidan Hunt, Abby Snortland, Brittany Lydon, Ama Hartman (and the many other folks that have been in and out of the lab) you have all made every day on campus (and in Zoom meetings) more enjoyable, and pushed me to think about problems in new and exciting ways. I especially enjoyed lab trips to Mazama, cider pressings in Winthrop, 4$^{\text{th}}$ of July's on Lopez, our daily lunch club, and the justice and equity group discussions. Further thanks to the many other students of ME who made BBQs, happy hours, intramural ultimate, studying for quals, and improptu games of racquetball so much more enjoyable.

My interest in marine energy was sparked during my Sophomore year technical writing course when I discovered that there was something called NNMREC - the Northwest National Marine Renewable Energy Center - here at UW. I reached out to two professors who did interesting looking work - Brian Polagye, and Jim Thomson. Lucky for me, Jim had a wave energy project that I could make plots in Excel for (and Brian didn't respond to me for three months), and the rest is history. Jim, I am so lucky to have worked in your lab for most of undergrad, I am grateful that you got me to think about going to grad school, and I look forward to working with you more in the future. Alex De Klerk and Joe Talbert, you are both incredible people and I am so grateful to have spent so much time working alongside you. I also appreciate the EFM group for welcoming me in as an undergrad with little research knowledge.

Outside of school, my family and friends helped support, encourage, and distract me. Chris and Amber, thanks for always being down for a ski trip and tailgate lunch. Mike and Hannah, you were both such trusty ski, adventure, and grilling buddies. Trevor and Ariana, sushi and sushi go, camping and biking trips, and dinners and birds have especially helped

me through the last year and half. Mandy and Gus, how lucky am I to have family who are also great friends. Holly and Ben, you were both such steady and kind roommates and friends. Sarah, you have been a constant source of joy, a dependable adventurer, patient, supportive, and inspiringly kind.I owe so much gratitude to my parents, Scott and Susan, for all they have done to support me, and for giving me free reign of their garden, a place that has been truly therapeutic throughout grad school. My Gram and Gramps taught me so much about hard work, and Gram, I try every day to make you more proud - and beat you at crib. The support provided by Nanny and Papa for my education is something I will also forever value.

And finally, thank you to Nirni Kumar, an original member of my committee who we lost far too soon. Nirni - you were the friendliest professor I ever had, you always took the time to stop, smile and say hi whenever I saw you on campus, you were funny and full of jokes, but could also talk for hours about any research question, all while making me feel like a peer rather than a student. You, your smiling face, and your cute dog brightened my general exam, and you are unbelievably missed.

Funding: Funding was provided by NSF GRFP under grant No. DGE-1762114 and Naval Facilities Engineering Command contract No. N0002410D6318 / N0002418F8702

DEDICATION

For my Gram

Chapter 1
INTRODUCTION

1.1 Wave energy converters

Harnessing power from the marine environment is an active area of research and development, with a growing emphasis on blue economy applications where the global presence of wave energy [10] provides compelling opportunities [16]. Wave energy converters (WECs) are devices that convert the power of ocean waves into usable forms of energy, such as electricity. This emerging technology has the potential to spur development of new activities at sea and, at a larger scale, diversify generation on the electrical grid. One archetype for these WECs is a point absorber, characterized as a device with a wave-actuated component much smaller than one ocean wavelength [6]. These devices consist of a surface float connected to a reaction body or seafloor anchor. The use of a reaction body free from the seafloor allows for operation of the devices in deep water and free-drifting configurations. This architecture, generically shown in Fig. 1.1, is the focus of my research, and provides a rich domain for study. Advancement of this technology requires accurate knowledge of forces on the system, and the ability to adequately model device dynamics. The emphasis of this dissertation is on the heave plate hydrodynamics.

1.2 Hydrodynamic forces in oscillatory flow

Over 150 years of research informs our current understanding of oscillatory hydrodynamics. Foundational work by Stokes [31] and Basset [2], who studied the motion of a submerged spherical pendulum, established the complexity of this hydrodynamic problem. Work since has covered many different geometries and applications. Much of the recent work originated in the oil and gas industry, where calculations of force on cylindrical spars and damping plates

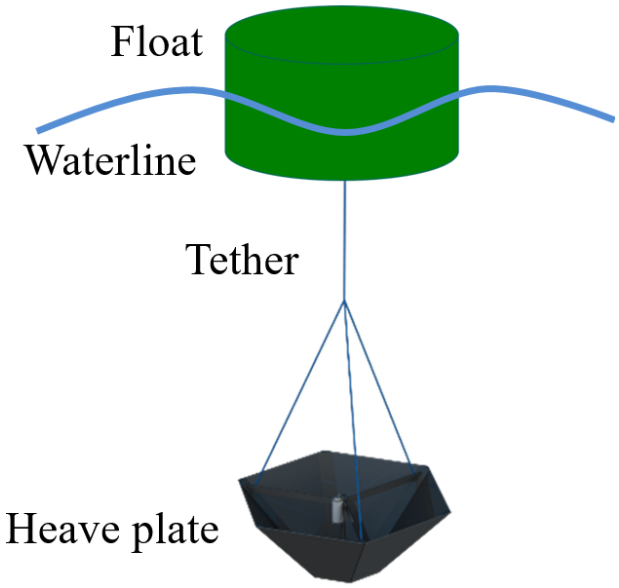

Figure 1.1: Representative point absorber wave energy converter.

were important for structural design and reduction of motion on deep sea oil platforms.

The hydrodynamic force (F_h) acting on an object in oscillatory flow is often decomposed into two component forces, drag (F_d) and added mass (F_a), written as

$$F_h = F_d + F_a. \tag{1.1}$$

This decomposition is referred to as the "Morison equation" [18]. The drag force is proportional to the squared velocity of flow past the body. Since we primarily focus on vertical heave motion, velocity ($\dot{z}$) will be referenced as the derivative of vertical position, z. We write the drag term as

$$F_d = \frac{1}{8} C_d \pi \rho D^2 \dot{z} |\dot{z}|. \tag{1.2}$$

where C_d is the coefficient of drag, ρ is fluid density, and D represents plate diameter. For non-circular plates, D is equal to the diameter of a circle with area equal to that of the body

being studied. We call this representation the "effective" diameter.

We can similarly write the added mass term as a product of a nondimensional added mass coefficient (C_a), fluid density (ρ), reference volume ($\pi D^3/6$), and acceleration ($\ddot{z}$). The reference volume is often taken as the displaced volume of the oscillating body, but for a thin body, we use the volume of a sphere with a diameter equal to the body's effective diameter. This representation is employed for all heave plate topologies considered in this dissertation. We can therefore write the added mass term as

$$F_a = \frac{1}{6} C_a \pi \rho D^3 \ddot{z}. \tag{1.3}$$

The Morison equation cannot describe all possible hydrodynamic forces arising in oscillatory flow and other decompositions have been proposed Sarpkaya and Isaacson [30]. The depth of a heave plate is such that it experiences negligible wave radiation, diffraction, and excitation forces, but forces due to vortices remain a possibility. Extensive debate exists around how to mathematically account for these effects. Competing theories typically add a third term to the Morison equation, but there are three different realizations of this third term.

First, Lighthill [15] accounted for the vortex force as a quadratic velocity term, grouped with drag. He writes that the forces may be approximated through the use of an ideal added mass coefficient and an experimentally determined drag coefficient. This is disputed by Sarpkaya [28], who notes that this neglects links between vortex behavior and fluid memory. Sarpkaya shows that the drag approximation accurately represents hydrodynamic forces only for small amplitude oscillations.

A second technique characterizes the vortex force through the use of an additional inertia term. This technique, similar to theory discussed by Basset [2], requires the use of an experimentally measured inertia term, an ideal fluid inertia component, and a drag term. This method, while providing a better approximation to the force for larger oscillations, still neglects any connection between vortex forces and velocity dependent forces [28].

As a result, Sarpkaya [29] suggests a third formulation: that the vortex force contains components proportional to both drag and inertia, making it difficult to separate from the drag and added mass terms of the Morison equation. Thus, the most accurate decomposition would include a third term proportional to some combination of velocity and acceleration. The mathematical complexity of such a decomposition leads to the suggestion by Sarpkaya and Isaacson [30], Sarpkaya [26, 27, 29] that the Morison equation, while theoretically incomplete, is sufficient for many ocean engineering problems. We therefore focus our analysis on traditional Morison decomposition and, but utilizing flow visualization to contextualize these hydrodynamics. We also revisit these theories as they relate to our results.

1.3 Nondimensional scaling of hydrodynamic forces on submerged bodies

Keulegan and Carpenter [12] were the first to explore the scaling implications of a traditional Morison decomposition for cylinders and flat plates in oscillatory flow. Importantly, they identify a dimensionless 'period parameter,' now known as the Keulegan-Carpenter number (KC), which describes the scaling of C_d and C_a. In the original work, this parameter is written as

$$\frac{U_m T}{D}, \tag{1.4}$$

where U_m is the maximum velocity of flow past the object during oscillation, and T is the period of oscillation. For sinusoidal oscillation, $U_m = 2\pi A/T$, where A is the amplitude of oscillation, so Equation 1.4 can therefore be written as

$$KC = \frac{2\pi A}{D}. \tag{1.5}$$

This reduction eliminates the dependence on frequency. It may also be evident that the KC number is the inverse of the Strouhal number.

Additionally, the Roshko number (Ro or β) is a non-dimensional oscillation frequency

and relates KC to the Reynolds number (Re) [33] as

$$Ro = \beta = \frac{D^2 f}{\nu}, \tag{1.6}$$

$$Re = \frac{U_m D}{\nu}, \text{and} \tag{1.7}$$

$$Re = (KC)\beta = \frac{2\pi A}{D}\frac{D^2(1/T)}{\nu} = \frac{2\pi AD}{\nu T}, \tag{1.8}$$

where f is the oscillation frequency in rad/s and ν is the kinematic fluid viscosity in m^2/s. We use β and Re to assess hydrodynamics scaling effects secondary to KC.

Tao and Dray [32] studied heave plates to reduce the motion of offshore structures. This study focused on the effect of porosity on hydrodynamic coefficients of flat heave plates, using a Morison decomposition. They found that higher porosity increased drag coefficients at low KC, but decreased drag at high KC. In contrast, more porous plates exhibited reduced added mass coefficients for all KC.

Two studies using a modified Morison equation with linear damping in place of quadratic drag. Garrido-Mendoza et al. [8] first used numerical methods to analyze added mass and damping coefficients as a function of plate submergence depth. Both coefficients increased when oscillations occurred "near" a seabed or free surface, and damping coefficients were related to calculated enstrophy, the integral of vorticity over a surface. In subsequent work, Garrido-Mendoza et al. [9] used flow visualization and force measurements from heave plate oscillation to validate the numerical simulation. These studies concluded that hydrodynamics become independent of depth when the oscillation midpoint is at least one object diameter from the surface. These results, however, were limited to oscillations with $KC < 2$.

More recent work by Bezunartea et al. [4] focused on a heave plate used to reduce the motion of a floating offshore wind turbine. They analyzed the scaling of drag and added mass coefficients for three sizes of flat circular plates. Coefficients of drag and added mass were found to depend only on KC and were independent of frequency and physical scale. Further, they showed that a linear damping coefficient was both scale and frequency dependent. In an effort to reduce scale and frequency dependence, we focus on a quadratic drag term, rather

than a linear damping term, to capture viscous effects in the flow.

1.4 Studies of heave plate hydrodynamics for point-absorber WECs

Recently, studies of oscillatory hydrodynamics have expanded to two-body point absorber WECs (e.g. Fig. 1.1). Beatty et al. [3] studied a two-body WEC that used a rigid column to connect heave plate to floating body, comparing the performance with and without a damping plate. This hydrodynamic comparison showed a drastic increase in added mass when using a damping plate, which shifted the period of peak power production towards that of more typical ocean waves. Additionally, in conjunction with a control scheme, the reduction of high frequency motion increased power output. This demonstrated the effectiveness of heave plates for point absorber WECs.

Brown et al. [5] characterized the hydrodynamics of both asymmetric and flat heave plates under forced oscillation. These plates were designed for the "miniWEC", a point absorber consisting of a cylindrical float, connected by tether to a submerged heave plate, much like the device shown in Fig. 1.1. Drag and added mass depended primarily on KC and weaking on the frequency of oscillation for both geometries. However, a reconstruction of total forces from the Morison equation was found to underestimate the peak hydrodynamic forces. This suggested that the decomposition did not capture all forces present in the system.

WEC developer Oscilla Power also studied asymmetric heave plates for two-body point absorbers. Mundon et al. [19] measured hydrodynamic force using a 1:50 scale plate, and compared the results with CFD. They found drag and inertia approached a constant value as Reynolds number was increased. Results also suggested a Reynolds dependence for the smallest plates for tests with $KC < 2$, indicating a minimum scale at which KC scaling applies. Additionally, they found good agreement between hydrodynamic forces calculated from CFD and measured experimentally for $KC > 2$. Rosenberg et al. [23] modeled and tested a prototype two-body WEC with an asymmetric heave plate. They compared numerical and experimental results for full system response in survival conditions (high amplitude waves). They found that, in some cases, dynamical models provided more accurate estimates

of device loads than CFD, with significantly lower computational cost. Additionally, they determined that dynamical models and CFD both under-predicted peak device loads in high amplitude waves.

1.5 Wave energy converter modelling

Due to the cost of experiments and the wide range of candidate technologies, simulation plays an important role in the development of WECs. My work focuses on results in the time-domain, but frequency-domain modelling is also commonly used when WEC performance is assessed across a large range of sea states. In the time-domain, two main approaches prevail in WEC simulation: computational fluid dynamics (CFD) and dynamical models.

CFD is occasionally used in situations where high accuracy is required and the assumptions required for lower-cost simulations may be invalid. Wei et al. [36] has shown success modelling an oscillating surge WEC in operational and storm conditions using smooth particle hydrodynamics (SPH). Rosenberg et al. [23] used Reynolds-averaged Navier-Stokes (RANS) modelling in the commercial code STAR-CCM+ to simulate a point absorber WEC in extreme seas. CFD modelling, especially for geometrically complex WECs, is computationally expensive, prohibiting full simulation of all operational conditions.

Dynamical models trade high accuracy for lower computational cost, allowing for simulation of complex devices across a wide range of sea states and device parameters. They rely on prior knowledge of device hydrodynamics to simulate WEC response in the time domain. Often, frequency-domain Boundary Element Method (BEM) solvers such as NEMOH [1] or WAMIT [35] are used to pre-calculate hydrodynamics of simulated devices. Open source code (e.g., WEC-Sim [37]) then uses BEM as an input to generate time-domain simulations of a WEC. Commercial codes ProteusDS [7] and OrcaFlex [21] use BEM results or empirically derived coefficients as inputs for time-domain simulations.

Because WEC hydrodynamics violate the irrotational flow assumption for potential flow theory, dynamical models relying on BEM have inherent uncertainties, particularly for fully-submerged bodies, such as heave plates. However, higher-cost CFD methods do not neces-

sarily improve accuracy [23]. In general, dynamical models are likely to be most accurate in normal operating conditions for a WEC, and CFD models are likely to provide better estimates of WEC response in extreme conditions Li and Yu [14]. However, the relative increase in fidelity for dynamical models using empirical hydrodynamics in place of BEM is not well established in the literature. My work builds the knowledge base required for accurate dynamical modeling of two-body point absorber WECs, with an emphasis on the hydrodynamics of submerged heave plates.

1.6 Research objective

The objective of this work is to experimentally characterize the hydrodynamics of heave plates for WECs, develop a fundamental understanding of how those hydrodynamics vary with heave plate scale and topology, and assess the relative benefit of heave plate hydrodynamic parameterizations on WEC simulations.

In Chapter 2, we perform forced oscillation experiments on an asymmetric heave plate at three geometric scales. We characterize the hydrodynamic forces using phase-invariant and -dependent formulations of the Morison equation, and assess the accuracy of these parameterizations across a range of oscillation parameters. Using these techniques, in Chapter 3 we perform additional forced oscillation experiments to determine the effect of topology on heave plate hydrodynamics. This work specifically investigates the impact of enclosed fluid on the overall reaction force generated by an oscillating heave plate. In Chapter 4, we assess the impact of these heave plate hydrodynamic parameterizations on WEC simulations. Using field data from a two-body point absorber WEC, we validate dynamical and analytical models of the device in irregular waves. We further validate the physics of the analytical model across a range of regular waves using the higher-fidelity dynamical model. This enables us to utilize the analytical model to test the effect of low-, mid-, and high-fidelity parameterizations of heave plate hydrodynamics on simulations of this WEC. Finally, Chapter 5 concludes this work, discussing the implications of these results on WEC simulation and design, as well as identifying avenues for future work.

Chapter 2

HYDRODYNAMICS OF ASYMMETRIC HEAVE PLATES

In this chapter, we explore the hydrodynamics of an asymmetric heave plate at three geometric scales using forced oscillation experiments. We investigate scale dependence of phase-invariant drag and added mass coefficients estimated from the Morison equation. Then, we use a windowed Morison equation to estimate phase-dependent coefficients that, for some KC, are shown to provide a better description of hydrodynamic force. We conclude with a discussion of the implication of these results for WEC design. Much of the content of this chapter is from Rusch et al. [25], published in *Ocean Engineering*. Content already introduced in chapter 1 has been removed for brevity.

2.1 Morison Decomposition

We separate the hydrodynamic force acting on oscillating heave plates into components of drag and added mass using the Morison equation [18]. Combining Eqs. 1.1, 1.2 and 1.3, we can write the full Morison equation as:

$$F_h = \frac{1}{8}\rho\pi D^2 C_d \dot{z}|\dot{z}| + \frac{1}{6}\rho\pi D^3 C_a \ddot{z}. \tag{2.1}$$

The quantity $\frac{\pi D^3}{6}$ represents the volume of a sphere with the same effective diameter as the heave plate. C_a therefore represents the fraction of the mass of that hypothetical sphere accelerated by the heave plate. This spherical volume is arbitrarily used for flat plates, and we extend its use to this asymmetric shape.

From equation 1.2, we show that the coefficient of drag can be solved for as:

$$C_d = \frac{F_d}{\frac{1}{8}\rho\pi D^2 \dot{z}|\dot{z}|} \tag{2.2}$$

If the heave plate is oscillating in quiescent water, $\dot{z}$ is generally taken to be the velocity of the plate, though we note this is an approximation when the plate is oscillating in its own wake.

The added mass force represents the force from the acceleration of water surrounding the heave plate. From Eq. 1.3, the coefficient of added mass is defined as:

$$C_a = \frac{F_a}{\frac{1}{6}\rho\pi D^3 \ddot{z}} \tag{2.3}$$

where $\ddot{z}$ represents the acceleration of the heave plate through quiescent water. We utilize these coefficients to compare drag and added mass forces across heave plates of three different scales.

2.2 Methods

2.2.1 Experimental Setup

We perform a series of experiments on hexagonal conic heave plates at three different sizes using three experimental setups. The 'full-scale' plate, shown in Fig. 2.1, has an effective diameter of 2.72 m and is referenced as the 1:1 scale plate since it is the largest plate in this study and corresponds to the heave plate on the field-scale WEC described in Chapter 4. The two smaller plates, shown in Fig. 2.2, have effective diameters of 0.54 m and 0.27 m. We refer to these as 1:5 and 1:10 scale models, respectively. Critical dimensions for the three plates are reported in Fig. 2.3.

The three plates were forced in sinusoidal oscillation in quiescent water and forces were measured using an in-line load cell. The general layout of experimental setups is given in Fig. 2.4 alongside the WEC it emulates. As described subsequently, each heave plate scale

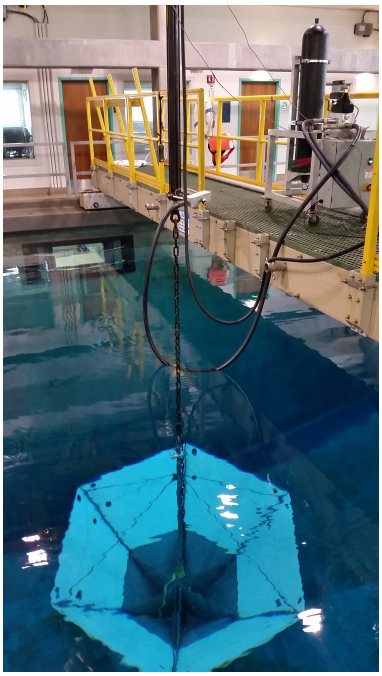

Figure 2.1: MBARI tank and 1:1 heave plate

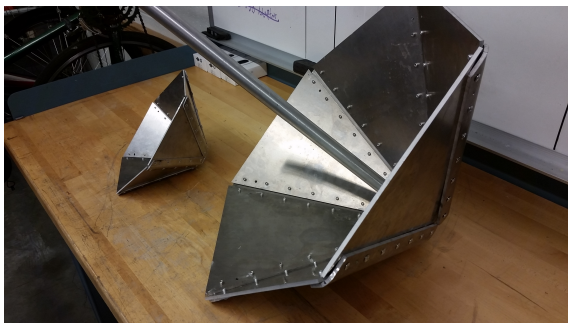

Figure 2.2: (left) 1:10 and (right) 1:5 open hexagonal conic heave plates

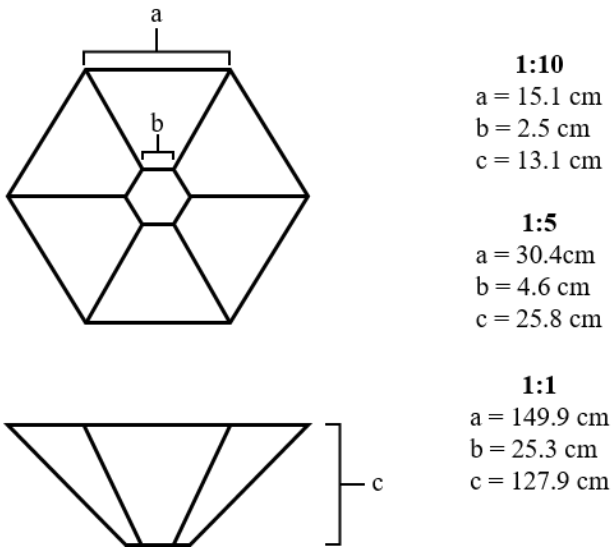

Figure 2.3: Measurements for experimental conic heave plates

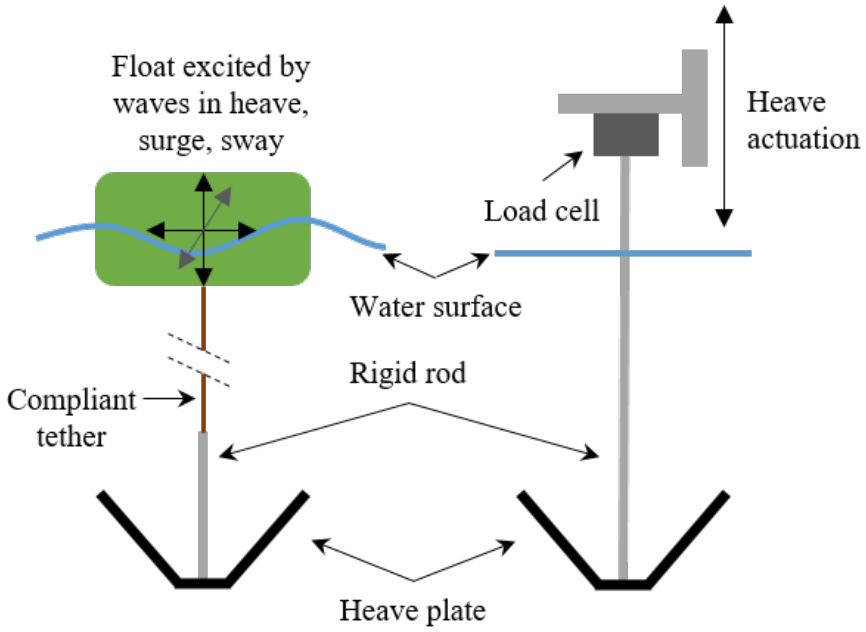

Figure 2.4: (left) Simplified two-body point absorber type wave energy converter and (right) general setup for forced oscillation experiments, which mimic the forcing on a heave plate by the WEC using an actuator. This simplification neglects non-heave forces or the effect of compliance in the tether between the WEC and heave plate.

Table 2.1: Overview of test parameters

	Facility			
	MBARI	Dockside		Lab Tank
Scale	1:1	1:5	1:10	1:10
KC	0.1 - 2	0.2 - 4.5	0.6 - 7.0	0.5 - 4.0
β ($\times 10^4$)	8.1 - 121	6.1 - 30.5	1.8 - 7.4	1.5 - 6.2
Re ($\times 10^4$)	11 - 71	6.5 - 28	4.2 - 20	2.8 - 9.1

was tested in a different facility. During testing, oscillation amplitude and period varied to cover a relatively wide, overlapping range of KC, β, and Re, as shown in Table 2.1, allowing us to validate conclusions across both scale and facility.

The Monterey Bay Aquarium Research Institute's (MBARI) test tank (Fig. 2.1) was used to characterize the full-scale plate. The tank is 12 m deep, 9 m wide, and 14 m long. A hydraulic ram with a 1.8 m stroke length is centered above the tank and actuates the heave plate using feedback position control. It is capable of 1.27 m/s speeds, with a maximum force of 2.7 kN. We measured force with a Honeywell model 45 load cell, which has a maximum rating of 44 kN and resolution of 22 N. Force and ram position were recorded at a rate of 200 Hz. During testing, the plate hung from the ram by chain and oscillation parameters were chosen to maintain chain tension throughout each test. Load cell sensitivity determined the minimum experimental amplitude and frequency.

The 1:5 and 1:10 scale models were tested at the University of Washington's Applied Physics Laboratory dock, using a modified setup from Brown et al. [5]. A belt drive linear actuator mounted at the dock's edge prescribes sinusoidal oscillations using feedback position control. From the carriage of the belt driven actuator, a Futek STL S-beam load cell with a 2.2 kN rating connects to a rigid driving rod, which suspends the plate 1.25 m beneath the free surface. As with the MBARI testing, force and position were recorded at 200 Hz. Oscillation parameters are limited by maximum actuator speed (≈ 0.65 m/s) and the signal-

to-noise ratio of the load cell, which required that period decrease with amplitude to maintain acceptable data quality, particularly for the 1:10 scale model.

The 1:10 scale model was also tested in a laboratory tank at the University of Washington measuring 1.5 m deep, and 1.3 x 1.3 m across. A ball screw linear actuator mounts above the center of the tank, and a rigid driving rod suspends the plate beneath the water surface. Velocity feedback control prescribes sinusoidal motion with a maximum stroke of 40 cm and a maximum speed of ≈ 0.65 m/s. An example of the commanded and realized position, velocity, and acceleration for this system is shown in Fig. 2.5 and demonstrates that the measured profile largely tracks the command. Aberrations at $\theta = 0$ and $\theta = 0.5$ result from mechanical backlash around zero velocity and exhibit no apparent effect on the calculated coefficients. A 0.24 kN 6-axis submersible load cell (ATI Mini 40) was installed at the interface between the heave plate and bottom of the driving rod. This acrylic tank was also used for flow visualization by releasing dye at the inside edge of the heave plate rim and capturing imagery at 60 frames per second with a camera (Nikon D3200 HD-SLR). To enhance dye visibility, processed images use only the blue color channel with the dynamic range truncated by MATLAB's "imagesc" function. Images are grouped by phase and averaged over realizations from five oscillations.

2.2.2 Data Analysis

Each experimental setup produces a time series of position and force. We analyze the hydrodynamic forces assuming both phase-invariant and phase-dependent behavior, and then assess the effectiveness of both approaches. We isolate quasi-steady oscillations (neglecting startup in quiescent water) before analysis. Tests using the dockside oscillator use sine waves with ramp-up and ramp-down periods that are discarded, leaving 40 oscillations for analysis. Tests in the MBARI tank and the UW test tank were limited to seven oscillations to minimize reflections, so oscillations use negative cosine waves with no ramp-up or ramp-down period. By removing the first oscillation, six quasi-steady oscillations remain for analysis.

The first step is to isolate the hydrodynamic force from the force measured by the load

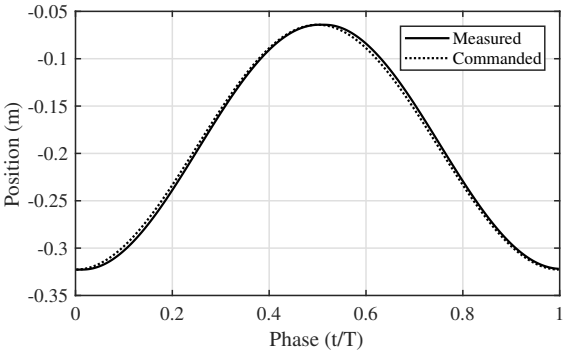

(a)

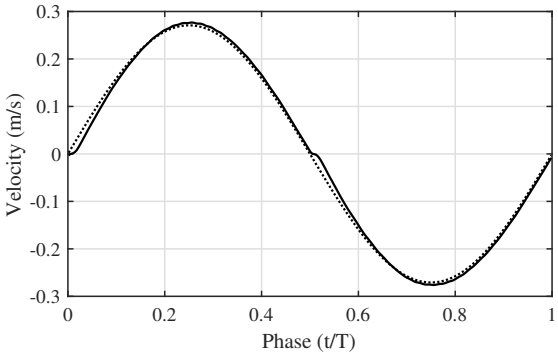

(b)

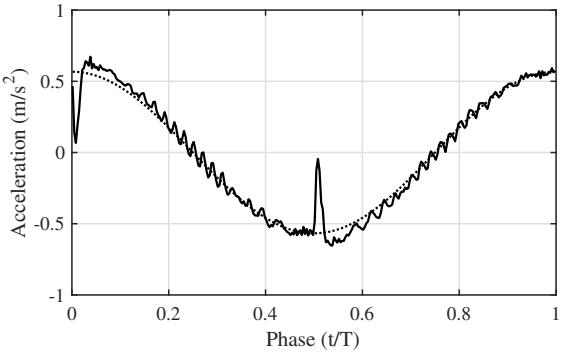

(c)

Figure 2.5: Commanded and measured (a) position, (b) derived velocity and (c) derived acceleration for the 1:10 plate in the UW tank, $KC = 3$, $T = 3$ s.

cells. Measured force is filtered using a low pass IIR filter with a 7 Hz passband frequency, 10 Hz stopband frequency, and 60 Hz stopband attenuation. For experiments at all three facilities, weight, inertia, and buoyancy of the heave plates must be accounted for and, for the MBARI tank and the dockside oscillator, so must the chain and driving rod. By deducting the force of inertia (F_i), weight (F_w) and buoyancy (F_b) from the filtered measured force ($F_{measured}$), we calculate the hydrodynamic force acting on the plate as

$$F_h(t) = F_{measured}(t) - F_i(t) - F_w + F_b(t). \tag{2.4}$$

The inertial force is estimated as

$$F_i(t) = \ddot{z}(t)(m_{hp} + m_{rod}), \tag{2.5}$$

where m_{hp} and m_{rod} are heave plate and driving rod masses, respectively. Heave plate acceleration ($\ddot{z}$) is calculated by twice differentiating heave plate position ($z(t)$). F_w is the product of m_{hp} and m_{rod} with gravity. The buoyancy force is given as

$$F_b(t) = \rho g(V_{hp} + V_{rod}(t)) \tag{2.6}$$

where V_{hp} and V_{rod} are the submerged volumes of the heave plate and driving rod (this volume changes throughout each oscillation), respectively, ρ is water density, and g is acceleration due to gravity. Consequently, the hydrodynamic force is given from measured force as

$$\begin{aligned} F_h(t) =& F_{measured}(t) - \ddot{z}(t)(m_{hp} + m_{rod}) \\ & -g(m_{hp} + m_{rod}) + \rho g(V_{hp} + V_{rod}(t)). \end{aligned} \tag{2.7}$$

The hydrodynamic force time-series (2.1) can be expressed compactly by representing inertial and drag terms with two constants, A and B, as

$$\begin{bmatrix} F_h(t_1) \\ F_h(t_2) \\ \vdots \end{bmatrix} = A \begin{bmatrix} \dot{z}_1|\dot{z}_1| \\ \dot{z}_2|\dot{z}_2| \\ \vdots \end{bmatrix} + B \begin{bmatrix} \ddot{z}_1 \\ \ddot{z}_2 \\ \vdots \end{bmatrix} \tag{2.8}$$

which can be solved for A and B using a least squares regression. Following this decomposition, the coefficient of drag is then

$$C_d = \frac{A}{\frac{1}{8}\rho\pi D^2} \tag{2.9}$$

and the coefficient of added mass is

$$C_a = \frac{B}{\frac{1}{6}\rho\pi D^3}. \tag{2.10}$$

Phase-invariant coefficients of drag and added mass are calculated from (2.8) using time-series data from all quasi-steady oscillations.

As noted by Sarpkaya [29], the hydrodynamic force may not be adequately described by only added mass and drag for some KC. Consequently, we evaluated the accuracy of this decomposition by reconstructing the force time series (i.e., treating F_h as the unknown in (2.8) and taking A and B as known constants). Comparison of this reconstructed approximation $\overline{F}_h$ to the measured F_h can identify portions of an oscillation where the Morison equation is inadequate. We focus on error in reconstruction of peak forces, which is the average of the normalized deviation between $\overline{F}_h$ and F_h at the 95^{th} and 5^{th} percentiles.

All time series data has been phase-averaged. Oscillation phase (θ) is defined as $\theta = t/T$, where $\theta = 0$ corresponds to the minimum oscillatory position, as shown in Fig. 2.5a. Phase bins with a width of $0.01T$ are used for averaging. We calculate phase-dependent coefficients of drag ($C_d(\theta)$) and added mass ($C_a(\theta)$). These coefficients are calculated from unfiltered

measured force, using (2.8) by partitioning the time series into windows of width $0.1T$, overlapping such that $C_d(\theta)$ and $C_a(\theta)$ maintain the same sampling rate as the measured data. θ is taken as the center of each window. This window size represents a compromise between phase resolution and experimental uncertainty. Force reconstruction using phase-dependent coefficients is denoted by $\widetilde{F}_h$. To preform this reconstruction, we first calculate coefficients $A(\theta)$ and $B(\theta)$ from $C_d(\theta)$ and $C_a(\theta)$, respectively, using (2.9, 2.10). Then, a phase-averaged reconstruction using phase-dependent coefficients can be constructed at each phase, θ_n, as

$$\widetilde{F}_h(\theta_n) = A(\theta_n)\dot{z}_n|\dot{z}_n| + B(\theta_n)\ddot{z}_n. \tag{2.11}$$

2.3 Results

We present results from all three plate scales in terms of phase-invariant hydrodynamics, phase-dependent hydrodynamics, and flow visualization. In Fig. 2.6a we see that phase-invariant C_d depends only on KC and is independent of Re, β or geometric scale in the evaluated regimes, consistent with the original findings of Keulegan and Carpenter [12] for oscillating flat plates. C_d exhibits high values for low KC, but approaches values typical of steady flow as KC increases. In Fig. 2.6b, C_a exhibits a scale-independent linear region for $KC < 1.5$, followed by a region with greater scale- and frequency-dependent variation that maintains Re independence. Keulegan and Carpenter [12] similarly find two trends in C_a across their tests, but do not explain why this change occurs.

Fig. 2.7 shows the degree to which a phase-invariant force reconstruction ($\overline{F}_h$) deviates from the measured hydrodynamic force (F_h) near the extremes in force where Brown et al. [5] found poor agreement. We observe that phase-invariant coefficients accurately represent the hydrodynamics at all tested scales for $KC < 1$, as the error in the peak force estimate is 10% or less. Error increases with KC and asymptotes around 25% for $KC > 2$. This suggests that at higher KC a phase-dependent decomposition may yield higher accuracy.

We focus our phase-dependent analysis on two test cases representative of different char-

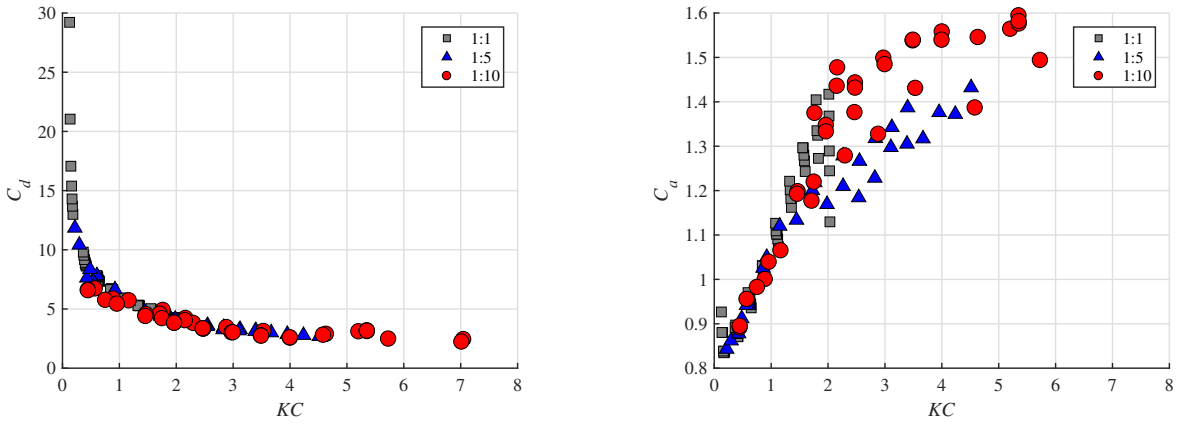

Figure 2.6: (a) Phase-invariant coefficient of drag (C_d) vs. KC and (b) added mass (C_a) vs. KC for all three heave plate sizes.

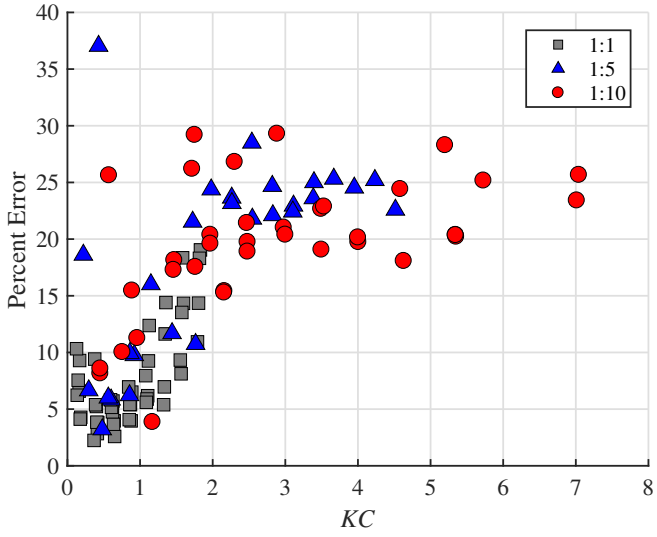

Figure 2.7: Percent error in reconstruction of peak forces using phase-invariant coefficients across all test cases.

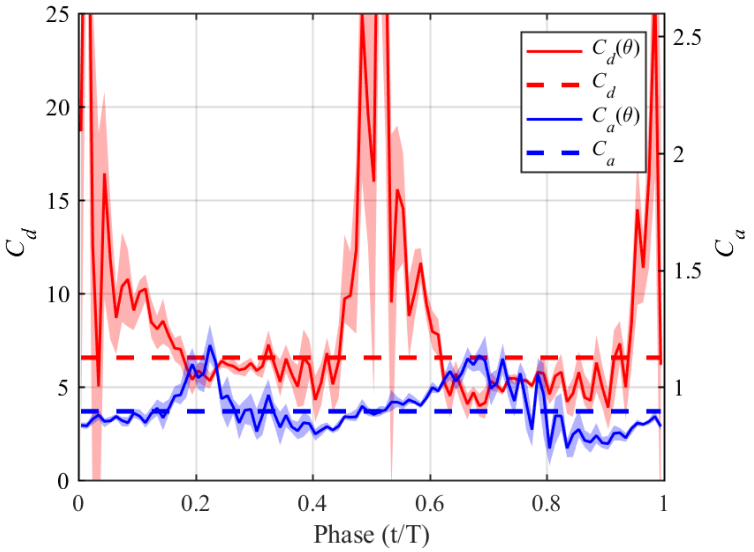

(a) $KC = 0.5$

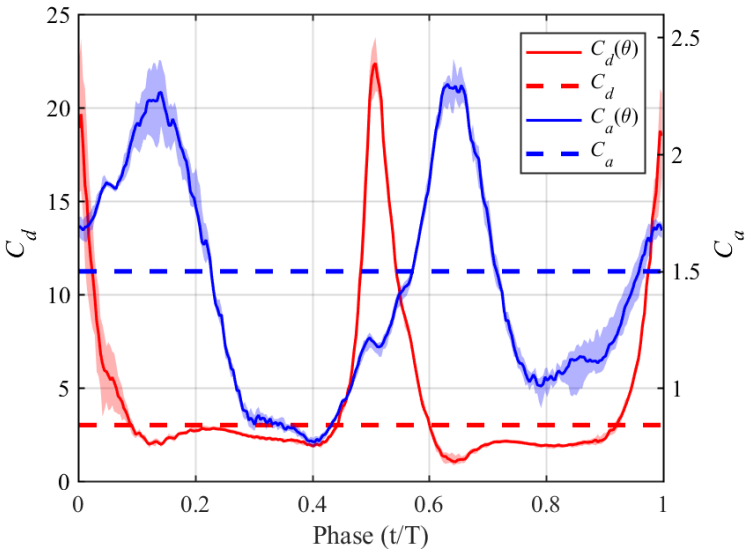

(b) $KC = 3.0$

Figure 2.8: Phase-dependent coefficients for a 1:10 plate, tested in the laboratory tank at (a) $KC = 0.5$, $T = 1$ s, and (b) $KC = 3.0$, $T = 3$ s. Shading denotes interquartile range for phase-dependent coefficients.

acteristic regions in Fig. 2.6b: $KC = 0.5$, representative of the linear region, and $KC = 3.0$, representative of the region of largest scale- and frequency-dependent variation in C_a. For $KC = 0.5$, shown in Fig. 2.8a, $C_d(\theta)$ is approximately equal to phase-invariant C_d except when the plate approaches zero velocity, a region where drag force is negligible. Similarly, $C_a(\theta)$ is approximately equal to phase-invariant C_a throughout the cycle. At larger KC, shown in Fig. 2.8b, $C_d(\theta)$ also behaves similarly to phase-invariant C_d, while $C_a(\theta)$ exhibits high variability. Potential flow theory anticipates no phase variability in C_a, but assumptions required for potential flow are increasingly violated with increased oscillation amplitude.

To assess the effectiveness of these two methods across KC, we compare the phase-averaged reconstructed hydrodynamic force using phase-dependent and -invariant coefficients, $\widetilde{F}_h$ and $\overline{F}_h$, respectively, with measured hydrodynamic force, F_h. In Fig. 2.9a ($KC = 0.5$), the reconstructions from both methods are in good agreement with F_h. This demonstrates that the Morison equation effectively describes hydrodynamic forces for $KC < 1$ and there is limited benefit to employing phase-dependent coefficients under these conditions. Conversely, phase-invariant reconstruction departs from measured forces in Fig. 2.9b ($KC = 3$), particularly during peak forces. However, $\widetilde{F}_h$ continues to match F_h, indicating high $C_a(\theta)$ variability shown in Fig 2.8b accurately parameterizes the inertial force for high oscillation amplitudes.

The contrast between consistent drag behavior and increased added mass variation as KC increases motivates a comparison of the magnitude of these terms in the overall hydrodynamic force. Fig. 2.10, which shows the ratio of the root mean square (rms) drag ($F_d(\theta)$) and added mass ($F_a(\theta)$) forces from phase-dependent coefficients, demonstrates that added mass is dominant for low amplitude oscillations and remains so for all tests we conducted. Despite increasing C_a and decreasing C_d with increasing KC, the relative contribution of drag increases for higher amplitude motions due to the quadratic dependence on velocity. Regardless, the added mass term accounts for more than 50% of the hydrodynamic force for all KC tested and accounts for more than 75% of the hydrodynamic force at $KC < 1$. This emphasizes the importance of correctly parameterizing added mass over the entire range of

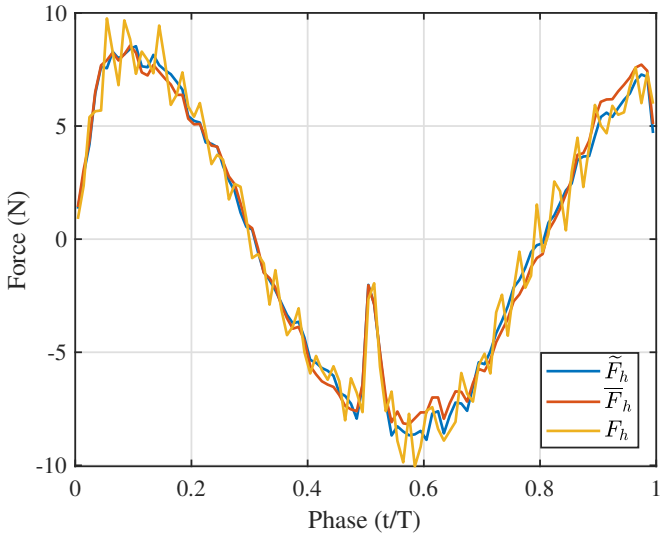

(a) $KC = 0.5$

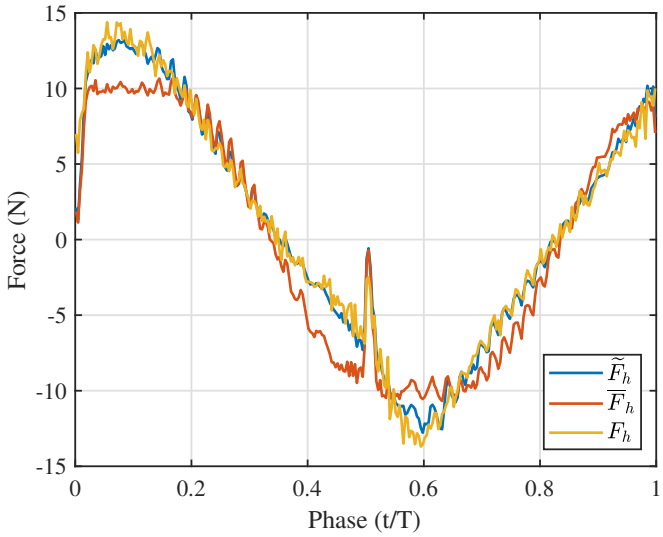

(b) $KC = 3.0$

Figure 2.9: Reconstruction of hydrodynamic force (F_h) using phase-dependent ($\widetilde{F}_h$) and phase-invariant ($\overline{F}_h$) coefficients for a 1:10 plate, tested in the laboratory tank at (a) $KC = 0.5$, $T = 1$ s, and (b) $KC = 3.0$, $T = 3$ s.

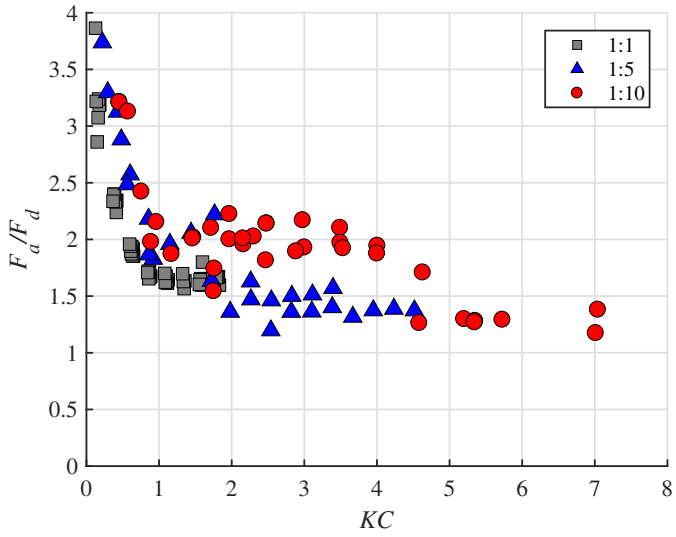

Figure 2.10: Ratio of the root mean square (rms) of the added mass force to the rms of the drag force versus KC for all tests, demonstrating the relative contributions to the total hydrodynamic force.

KC of operational interest.

For a qualitative look at the vortex dynamics in these flows, we injected dye during oscillations of the 1:10 plate. The image sharpness (i.e., lack of blurring) in the phase-averaged images of Fig. 2.11 indicates cycle-to-cycle consistency in the coherent flow structures, consistent with the relatively small inter-quartile ranges for phase-dependent force coefficients (Fig. 2.8). There is a clear evolution of vortex formation and shedding with distinctive differences between KC at each phase. The change in phase-invariant C_a and the increased range of $C_a(\theta)$ with increasing KC may suggest a weak link between vortex behavior and inertia. As discussed by Sarpkaya [29], the Morison equation cannot capture the vortex force, which may be important for some KC. However, the vortex structures around the plate (Fig. 2.11) suggest that such forces are present for an oscillating, asymmetric heave plate and that the differences in vortex formation across KC are likely to affect Morison equation fidelity. We therefore present these images alongside phase-dependent $C_a(\theta)$ to show that, while we expect added mass to maintain a constant value, additional force is included by

default in this acceleration-dependent term. The rise and fall of the resulting $C_a(\theta)$ term is loosely linked to the growth and destruction of a vortex near the plate, indicating vortex forces may be impacting the inertial term in a manner similar to a history or "Basset" term [30, 2].

2.4 Discussion

2.4.1 Morison equation fidelity

The similarity of $\overline{F}_h$, $\widetilde{F}_h$, and F_h at $KC < 1$ indicates that phase-invariant coefficients accurately represent the hydrodynamic forces for small-amplitude oscillations. Therefore, the Morison equation can be used to represent the time-variation in hydrodynamic forces of an asymmetric heave plate in this region and any other forces (e.g., the "vortex force") are negligible. This is consistent with observations by Sarpkaya and Isaacson [30], who note that vortex forces are not significant for cylinders in oscillatory flow at low KC. Similarly, McNown and Keulegan [17] identify a ratio of oscillation frequency to vortex shedding frequency above which separation and vortex shedding become important. For $KC < 1$ in our experiments, the frequency ratio remains below this threshold, such that we would not expect vortex forces to influence the hydrodynamics.

Conversely, for $KC > 3$, phase-invariant coefficients cannot accurately estimate the hydrodynamic force at some phases of oscillation, including the phases where hydrodynamic force is at a maximum. The phase-dependent force reconstruction, $\widetilde{F}_h$, does track the hydrodynamic force, demonstrating that a modified Morison equation with phase-dependent coefficients is able to predict hydrodynamic force throughout an oscillation.

As discussed extensively by Sarpkaya [26, 27, 28, 29], Sarpkaya and Isaacson [30], secondary forces such as the vortex force may depend on higher order terms beyond linear acceleration and quadratic velocity. In our experiments, secondary forces are seen to be parameterized primarily by $C_a(\theta)$, because $C_d(\theta) \approx C_d$. Fig. 2.11 generally shows vortex development while $C_a(\theta)$ increases and vortex shedding while $C_a(\theta)$ decreases. While Sarpkaya

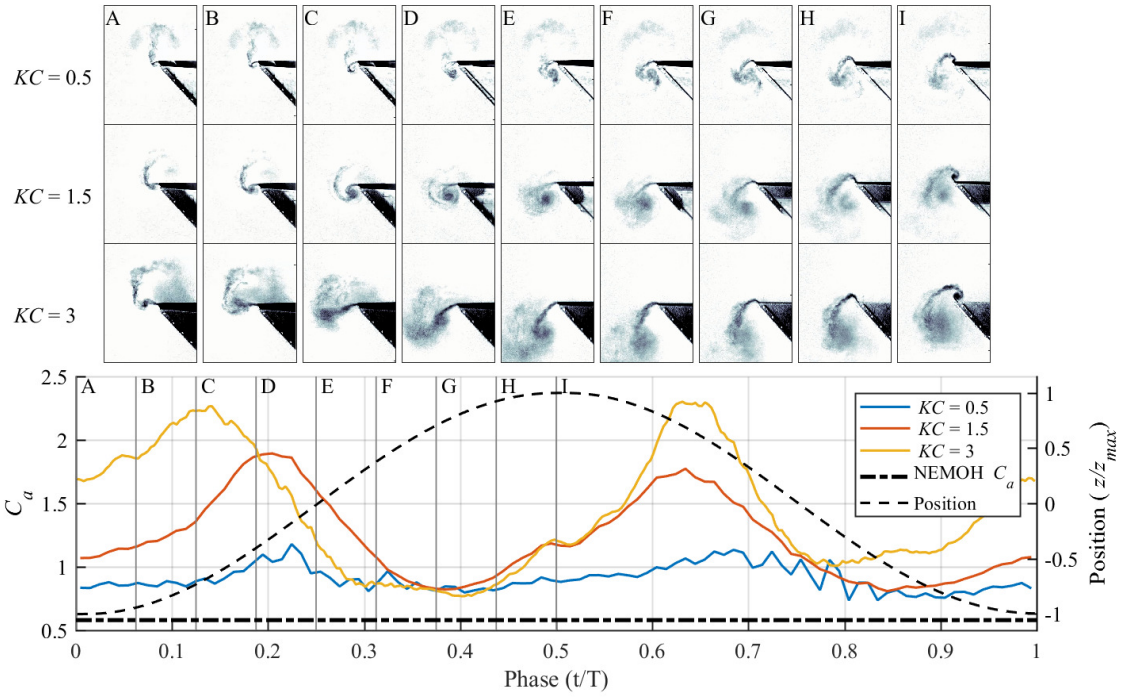

Figure 2.11: (top) Flow visualization for upstroke ($\theta = 0$ to $\theta = 0.5$) of 1:10 heave plate in the laboratory tank at $KC = 0.5$, 1.5, and 3. (bottom) Phase-dependent added mass coefficients. Vertical lines correspond to each lettered image column. The sinusoidal dashed line shows the plate position and the horizontal dash-dot line denotes the added mass coefficient calculated by NEMOH.

and others have described the vortex force by adding a third term to the Morison equation, and Lighthill [15] suggests that the vortex force should be parameterized with drag, our results suggest that this force can be approximated by the two term Morison equation with a phase-dependent added mass coefficient. For consistency with theory, this might be better conceptualized as the sum of a phase-invariant added mass coefficient and an additional phase-dependent "inertial coefficient", along the lines of a history term or Basset force.

2.4.2 Implications for wave energy

WECs may be designed for a variety of sea states and operating conditions, and heave plates may, therefore, experience a wide range of KC. Understanding the average and maximum forces present across sea states is key to the design and control of two-body WECs. As shown in Table 2.1, our experiments spanned $KC = 0.1$ to $KC = 7.0$. While it is conceptually attractive to consider "low" KC values as representative of low-energy sea states and "high" KC values as storm conditions, the amplitude of heave plate motion depends strongly on the specific design of the WEC and the control strategy employed. With this in mind, we contextualize our results to wave energy conversion. Specifically, as part of the design validation for a two-body WEC, a developer should evaluate and consider the impact of the KC regime on the fidelity of predicted hydrodynamics forces. Such a validation step is warranted regardless of heave plate geometry.

For low-amplitude motions ($KC < 1$), phase-invariant coefficients accurately describe the forces on an asymmetric heave plate. While C_d decreases rapidly as KC increases in this regime, C_a varies linearly over a small absolute range and inertial forces are dominant. Consequently, heave plate hydrodynamic forces should be predicted with reasonable accuracy in this range using single-value representations of C_d and C_a.

Conversely, error in force prediction using phase-invariant coefficients increases with KC when $KC > 1$. At higher KC, C_d asymptotically approaches a constant value. However, C_a scatters above $KC = 2$, with a weakly asymptotic, scale-dependent trend and, in this regime, inertial forces continue to dominate. As a result, while a narrow range of C_d values would adequately parameterize drag forces, we expect inertial forces in this regime to be more difficult to estimate, particularly if obtained from scale model experiments. Our results show that, for $KC > 1$, we would under-predict peak loads on an asymmetric heave plate by up to 30% if using phase-invariant coefficients. Peak loads are important to WEC development because they drive decisions about structural design and hence impact overall cost.

These results highlight a challenge for predicting loads on two-body WECs when heave

plate $KC > 1$. A number of simulation tools are commonly used by wave energy developers, including Orcaflex (Orcina), ProteusDS (DSA), and WEC-Sim (Sandia and NREL). While we have shown that hydrodynamic force is accurately reconstructed across all KC using phase-dependent coefficients, these tools have, at best, a limited ability to incorporate phase-dependent coefficients and, therefore, cannot accurately represent peak forces for high-amplitude motion of asymmetric heave plates.

Further, phase- and scale-invariant added mass coefficients in these simulations often rely on predictions from Boundary Element Method (BEM) solvers, rather than physical measurements. To contrast BEM estimates with our experimental results, we calculated added mass using NEMOH, an open-source linear potential flow solver [1]. For these calculations, we conducted a mesh convergence study and took as representative the asymptotic added mass coefficient for simulations with greater than 700 panels. The plate was submerged 20 m beneath the free surface (deep water assumption). For the 1:10 plate, NEMOH predicted an added mass coefficient of 0.58, with a similar value reproduced in WAMIT. As shown in Fig. 2.11, this is lower than phase-dependent and phase-invariant C_a values for all experiments. Since potential flow theory assumes irrotational flow, this error in added mass could be anticipated from the vortical structures formed during oscillation.

There are indications that this under-prediction of added mass is not improved by higher fidelity methods as Mundon et al. [19] conclude that CFD similarly under-predicts loads for an asymmetric reaction body. Further work by Rosenberg and Mundon [22] demonstrated that despite its high computational cost, CFD provides little to no improvement over BEM. Continued efforts to improve these models are therefore critical, and these challenges demonstrate the value of physical experiments to characterize added mass.

Finally, in the context of wave energy, a few motivations exist for the use of a three dimensional asymmetric heave plate. Flat heave plates may experience a “falling leaf” motion, with side to side motion during vertical oscillation. As observed by our collaborators at MBARI, the asymmetric plate studied here limits that horizontal motion during the downstroke. Further anecdotal motivation for an asymmetric shape is potential “snap load” mitigation. Snap

loading may occur when a WEC uses a compliant connection between the surface float and heave plate. If the heave plate descends more slowly than the float, such that slack develops in the tether, there is a large, transient force when the tether returns to tension, posing a risk of structural damage. By generating asymmetric hydrodynamics, which provide less resistance during the downstroke, a plate could reduce the probability of snap loading. However, as shown in Fig. 2.10, the inertial forces constitute the majority of hydrodynamic force for all KC tested and Fig. 2.9 demonstrates that added mass forces do not depend on the direction of plate motion. $C_d(\theta)$ is higher during the upstroke ($t = 0 - 0.5T$) than the downstroke (Fig. 2.8b), but this difference is minor and the resulting hydrodynamic force is only weakly asymmetric. Our results suggest that, while asymmetric heave plate geometry may reduce lateral motion during operation, it is unlikely to significantly reduce the probability of snap loading.

2.5 Conclusions

Through experiments, we have shown that phase-invariant drag and added mass coefficients generally scale with KC for asymmetric heave plates. This demonstrates that similar trends for cylinders and flat plates can be extended to novel, asymmetric geometries. Further, these results indicate that scale-model experimental characterization of small-scale heave plates produce phase-invariant coefficients representative of larger plates.

Consequently, the two-term Morison equation with phase-invariant coefficients is likely sufficient for estimating heave plate forces in this region of motion. For $KC > 1$, we show that phase-invariant coefficients do not adequately describe the hydrodynamic force, particularly during times of maximum loads. This is primarily due to large deviations in $C_a(\theta)$ from C_a. We therefore suggest that WEC developers pay careful attention to the KC range of their heave plates and that commercial code developers consider supporting a modified form of the Morison equation that allows a phase-dependent inertial term.

Finally, our observations of a two-term representation of oscillatory hydrodynamics ascribes error in the Morison equation primarily to the inertial term. Flow visualization sug-

gests that vortex development and shedding is loosely correlated with observed trends in $C_a(\theta)$. This suggests that a phase-varying inertial term accounting for deviation from C_a may accurately account for the vortex forces on the plate. This result may warrant further consideration and theoretical development.

Chapter 3

HEAVE PLATE TOPOLOGY

The goal of this chapter is to investigate the effect of heave plate topology on fluid reaction forces, with a specific focus on identifying the impact of enclosed fluid on the reaction force of a hexagonal conic plate. Through this work we also identify asymmetric vortex dynamics that yield asymmetry in hydrodynamic forces for a symmetric, flat plate. This work has been submitted for publication in *Ocean Engineering*. Information discussed in the preceding chapters has been removed from this chapter to avoid repetition. In particular, this chapter relies upon much of the same theory as Chapter 2.

3.1 Introduction

While prior work has compared the reaction force for two-dimensional to three-dimensional topology [5], the role of fluid inertia constrained by plate topology remains unclear (i.e., fluid trapped within a structure). We experimentally characterize fluid reaction forces for three heave plate topologies depicted in Fig. 3.1: a flat, hexagonal plate ("flat plate", Fig. 3.1a), an open, hexagonal conic plate ("open conic", Fig. 3.1b), and a topology created by enclosing the open conic with the flat plate ("enclosed conic", Fig. 3.1c). We describe our experimental method and an overview of our data analysis techniques and present the Morison equation decomposition in both a phase-invariant and phase-dependent sense. This addresses an existing literature gap in the effects of enclosing fluid within a concave heaving body and provides guidance to WEC developers on selecting an appropriate heave plate topology. In addition, we explore a hydrodynamic asymmetry that occurs for the flat plate (KC = 1-2) and is correlated with asymmetry in observed vortex dynamics.

(a) (b) (c)

Figure 3.1: Three experimental test articles with varying topology: (a) flat plate, (b) open conic, and (c) enclosed conic.

3.2 Methods

3.2.1 Experimental setup

Experiments were conducted in a transparent acrylic tank, measuring 1.5 meters tall with a 1.3 m by 1.3 m base (Fig. 3.2). An external frame supported a screw driven linear actuator (Parker HMRS11), which provided a 40 cm maximum stroke and 65 cm/s maximum velocity. Heave plate position was measured by an encoder integrated with the actuator. Heave plates were attached to a solid rod coupled to the actuator, which prescribed regular sinusoidal motion through velocity feedback control. A submersible, six-axis load cell (ATI Mini40) was mounted between the heave plate and driving rod to measure reaction forces. Both position and reaction forces were recorded at 1000 Hz by a DAQ (NI DAQ model 6351) connected to a computer running MATLAB.

We initialized experiments in quiescent water and, between tests, waited 1-2 minutes for residual fluid motion to subside. Measured load cell forces returned to their quiescent noise floor within seconds, but suspended particles in the water took longer to come to rest. As with experiments in Chapter 2, and depicted in Fig. 2.5a, we initiated plate motion from

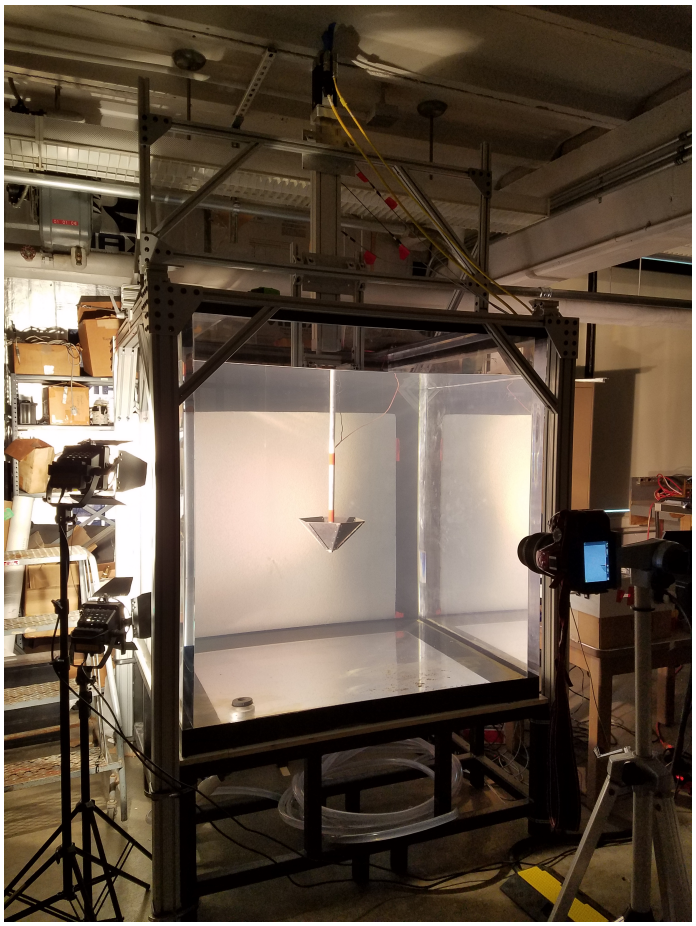

Figure 3.2: Experimental flow visualization tank. The heave plate (an open hexagonal conic) is suspended in the tank from a linear actuator.

the bottom of the oscillation stroke for most experiments. Starting from zero velocity allows the actuator to immediately begin the full oscillation shown in Fig. 2.5b. We refer to the location within an oscillation as the "phase", $\theta = t/T$, where t is time and T is period. For a subset of experiments, tests were initialized at the top of the oscillation stroke ($\theta = 0.5t/T$) and these cases are explicitly noted in the results. For those tests, $\theta = 0.5$ continues to refer to the apex of the oscillation stroke for phase-averaged comparisons with tests initiated at $\theta = 0$. All experiments consisted of ten oscillations, but only the last eight were included in analysis to remove any influence of the transient response.

3.2.2 Hydrodynamic analysis

As in Chapter 2, velocity ($\dot{z}$) and acceleration ($\ddot{z}$) are calculated by differentiating plate position (z), yielding a slight increase in noise with each step (Fig. 2.5). Measured force (F_{measured}) is filtered using a low-pass IIR filter with passband and stopband frequencies of 7 and 10 Hz, respectively, to eliminate electrical noise in the signal. F_{measured} consists of five components: hydrodynamic forces (F_h), inertia from enclosed fluid ($F_{i,\text{enclosed}}$), inertia from plate mass ($m_{\text{hp}}\ddot{z}$, where m_{hp} is heave plate mass), plate weight ($m_{\text{hp}}g$, where g is gravity), and plate buoyancy (F_b). This balance of forces is expressed mathematically as

$$F_{\text{measured}} = F_h + F_{i,\text{enclosed}} + m_{\text{hp}}\ddot{z} + m_{\text{hp}}g - F_b. \tag{3.1}$$

This is an augmentation of Eq. 2.4 that expands the inertial force term to include the inertia from enclosed fluid. As before, F_h is the only unknown term in Eq. 3.1 and the term of primary interest in these experiments. $F_{i,\text{enclosed}} = 0$ for the flat and open conic, and can be calculated for the enclosed conic given the flooded volume of the topology and density of water. For much of our analysis, we group F_h and $F_{i,\text{enclosed}}$ together as the "fluid force" ($F_{\text{fluid}} = F_h + F_{i,\text{enclosed}}$) to make equivalent comparisons across the three topologies. We then apply the Morison equation [18] to the hydrodynamic force as in Chapter 2.

For purposes of comparing reaction forces across topologies, we define a "fluid inertia

coefficient" that includes the enclosed fluid inertia by augmenting Eq. 2.10 as

$$C_{fi} = \frac{B + m_{w,\text{enclosed}}}{\frac{1}{6}\rho\pi D^3}, \tag{3.2}$$

where $m_{w,\text{enclosed}}$ is the mass of enclosed water calculated from ρ and the interior volume of the enclosed conic. Since both added mass and enclosed fluid inertia are proportional to plate acceleration, C_{fi} parameterizes the total fluid inertia force (F_{fi}). For the flat plate and open conic, $m_{w,\text{enclosed}} = 0$ and $C_{fi} = C_a$.

While phase-invariant coefficients are commonly used in dynamic modeling software (e.g., ProteusDS, DSA, Ltd.), as shown in Chapter 2, these coefficients cannot accurately represent open conic hydrodynamic forces for some KC. Consequently, we first evaluate the accuracy of phase-invariant coefficients for all three plate topologies. We calculate a reconstructed force ($F_{h,re}$) by solving for the left side of Eq. 2.8 with the known time series of velocity and acceleration and the calculated constants A and B. We compare $F_{h,\text{re}}$ to F_h using an error metric (E_{re}) that emphasizes reconstruction errors during maximum hydrodynamic force. For wave energy applications, maximum hydrodynamic force ($\max(F_h)$) is important for structural design. Consequently, we define $\min(F_{h,\text{re}})$ as the 5^{th} percentile and $\max(F_{h,\text{re}})$ as the 95^{th} percentile and express the error metric as

$$E_{\text{re}} = \frac{1}{2}\left(\frac{|\max(F_{h,re}) - \max(F_h)|}{\max(F_h)} + \frac{|\min(F_{h,\text{re}}) - \min(F_h)|}{\min(F_h)}\right). \tag{3.3}$$

This represents the geometric average of the reconstruction error at the force extremes during oscillations. We note that because we are primarily interested in Morison decomposition accuracy, E_{re} is based on F_h, not F_{fluid}, as the latter choice would artificially increase accuracy for the enclosed conic due to the well-defined mass of the enclosed fluid, particularly at low KC.

Because the three topologies differ in their vertical symmetry (i.e., conics are asymmetric, plate is symmetric), we seek to understand how this asymmetry manifests in the fluid reaction

forces (drag and inertia). For this purpose, we calculate the ratio of rms fluid reaction force for the upstroke relative to the downstroke, as

$$F_{\text{fluid},va} = \frac{\text{rms}(F_{\text{fluid}}|0 \leq \theta \leq 0.5)}{\text{rms}(F_{\text{fluid}}|0.5 < \theta \leq 1)}. \tag{3.4}$$

$F_{\text{fluid},va} > 1$ corresponds to a greater fluid force on the upstroke than the downstroke.

While this can identify asymmetry in the fluid reaction force directly from measurements, to gain further insight, we need to decompose the hydrodynamic force within the upstroke and downstroke. Chapter 2 shows a phase-*dependent* Morison decomposition can accurately reconstruct hydrodynamic forces over a full oscillation. To calculate phase-dependent hydrodynamic coefficients, we set t_1 in Eq. 2.8 equal to the start of the first quasi steady oscillation, and $t_{\text{end}} = t_1 + 0.1T$. We perform a least squares fit on this subset of data, yielding representative constants A and B at the midpoint of this window (i.e., $t = t_1 + 0.05T$). We shift the window forward one timestep and repeat until reaching the end of the data set. This produces a time series of phase-dependent drag ($C_d(\theta)$) and added mass coefficients ($C_a(\theta)$). These values are then phase averaged over the eight non-transient oscillations by taking the median of data points at each oscillation phase and bin averaging in bins of width $0.1T$ to smooth cycle-to-cycle and phase-to-phase variations.

3.2.3 Flow visualization

In addition to force measurements, we visualized flow structures at the edge of the plate by injecting dye into the flow. A syringe filled with dye (food coloring) was connected to a length of flexible tubing (Tygon), which was routed along the driving rod and secured to the outer edge of the heave plate. Being hand-regulated, the dye flow-rates are unsteady and are only used to qualitatively assess flow structures (i.e., concentrations and corresponding image intensity are not indicative of absolute entrainment or mixing). Video of flow visualization was recorded with a camera (Nikon DSLR) outside of the tank at a 60 Hz frame rate.

We post-process these recordings to enhance interpretability. We re-scale the image

colormap (MATLAB imagesc), elevating the contrast of the dye against the background. We then phase average the video frames, calculating a mean image for each oscillation phase. This emphasizes periodic flow structures and minimizes irregular dye motion and artifacts introduced by hand injection. We finally subtract the median video frame to remove the background, leaving only time varying flow structures.

3.3 Results

We present our results in the context of the two different approaches to the Morison decomposition we employ: phase-invariant and phase-dependent. Because results are only weakly dependent on oscillation frequency (Chapter 2), they are presented solely as a function of KC number (Eq. 1.5).

3.3.1 Phase-invariant coefficients

The phase-invariant coefficients are shown in Fig. 3.3. The flat plate has the highest phase-invariant C_d, while the enclosed conic has the lowest, particularly at low KC. Fig. 3.3b shows that all three topologies have similar C_{fi} at low KC and that C_{fi} increases with KC for all topologies. The flat plate and open conic have similar C_{fi} over the range of KC, but the enclosed conic has a lower C_{fi} than the other topologies at high KC. The two conic topologies generally experience lower oscillation-to-oscillation variability, as shown by the whiskers on each data point. The higher variability for the flat plate is most evident in fluid inertia coefficient from $KC = 2.5 - 3.5$, highlighted by the insets in Fig. 3.3b.

As these are only phase-invariant *approximations*, they do not perfectly represent the observed hydrodynamics. As shown in Fig. 3.4, peak reconstruction error increases with KC. For $KC > 2$, the error approaches 20 - 25% for all plates, with little distinction between the topologies. Conversely, for all topologies, error falls to $< 10\%$ when $KC < 1$.

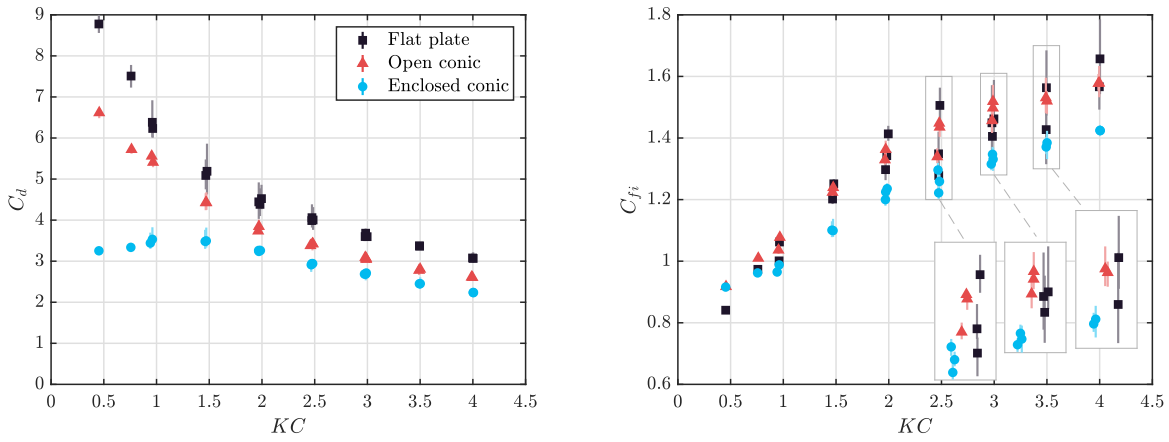

(a) (b)

Figure 3.3: (a) Phase-invariant coefficient of drag (C_d) vs. KC and (b) fluid inertia (C_{fi}) vs. KC for all three heave plate geometries. The "whiskers" (vertical lines) represent the range between maximum and minimum values of the phase-invariant coefficients over all oscillations. The inset figures in (b) are shown with an artificial offset in the x-direction to emphasize the differences in oscillation-to-oscillation variability for the topologies.

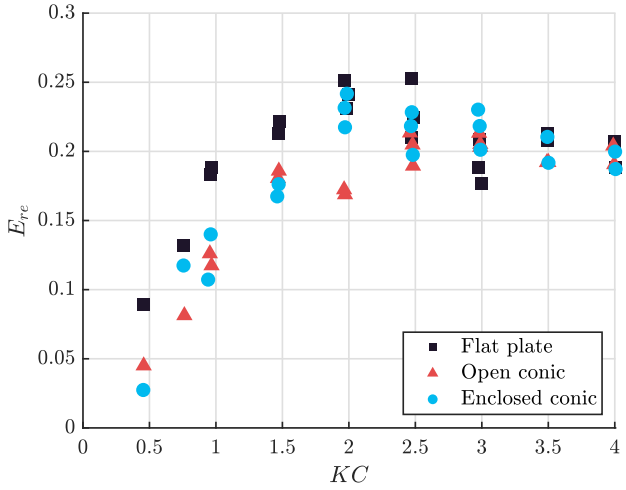

Figure 3.4: Phase-invariant peak reconstruction error (E_{re}) as a function of KC.

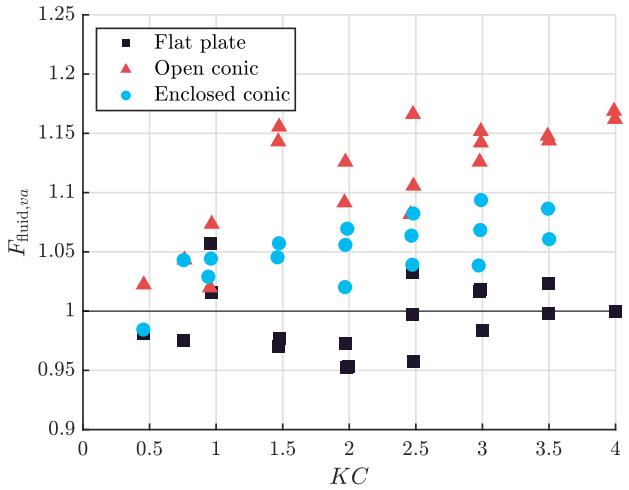

Figure 3.5: Vertical fluid force asymmetry ($F_{\text{fluid},va}$).

3.3.2 Phase-dependent hydrodynamics

As shown in Fig. 3.5, the open and closed conics both generate asymmetric fluid forces (Eq. 3.4). This asymmetry increases with KC to a maximum of about 15% for the open conic. The enclosed conic produces less asymmetry, and the flat plate remains within about 5% of a symmetric ratio for all KC.

3.4 Discussion

Our results demonstrate that a flat heave plate generates drag and added mass coefficients that are greater than or equal to the three-dimensional topologies tested. We further show that these phase-invariant representations are accurate for $KC < 1$, but that 20-25% error in peak force reconstruction is expected at higher KC. In the following section, we assess the breakdown of forces contributing to these results, their implications for heave plate design, and the limits to the phase-dependent Morison decomposition.

3.4.1 Comparison of forces

While we observe clear differences between hydrodynamic *coefficients* for each topology (Fig. 3.3), the absolute fluid force has the greatest impact on heave plate topology selection. As shown in Fig. 3.6, the flat plate produces a larger fluid reaction force for nearly every experiment, though the open conic produces only slightly less reaction force (within 10%). Counter to our expectations prior to these experiments, enclosing a moderate fluid mass within the conic significantly reduces the fluid reaction force.

Fig. 3.7 shows the breakdown of total reaction force (defined as a sum of the time-varying forces acting on each plate) for a representative case. Despite the lower structural inertia forces for the flat plate, larger fluid forces produce greater overall reaction forces. In other words, it would be more effective to generate greater reaction forces by using the additional material in the conic to increase the diameter of a flat plate. In general, structural inertia is small in comparison to the fluid force. We also highlight the contribution of enclosed fluid inertia to the overall fluid force of the enclosed plate. This term provides more force than structural inertia, but does not represent a significant contribution to total fluid force. In fact, enclosing the conic plate reduces the drag and added mass forces, in turn reducing the total fluid force.

The flat plate also generates larger maximum forces for many of the experiments, including the case highlighted in Fig. 3.7. As shown in Fig. 3.7b, the flat plate produces a maximum force 5% greater than the open conic, and 14% greater than the enclosed conic. We note that the individual forces do not sum to the total reaction force, since drag and inertia are out of phase. This is why the open conic plate produces a lower maximum total reaction force despite generating a maximum added mass force 25% larger than the flat plate.

3.4.2 Implications for heave plate selection

These results clearly demonstrate that flat plates generate larger reaction forces than the other two topologies. Given that flat plates require less material and are less complicated

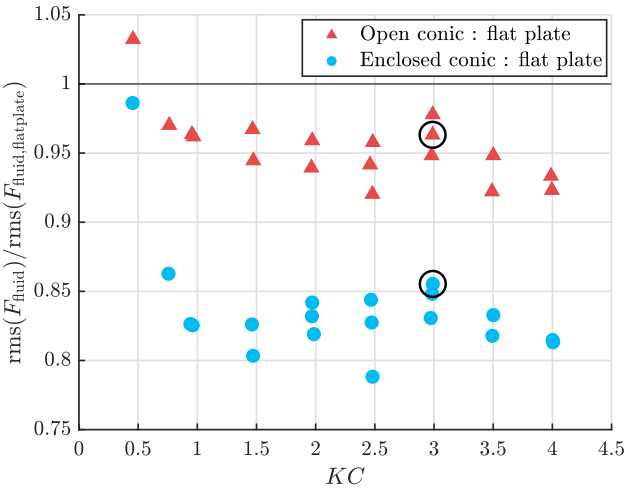

Figure 3.6: Ratio of rms fluid force for each three-dimensional topology relative to the flat plate at equivalent experimental parameters. The circled points are shown in greater detail in Fig. 3.7

to manufacture, they appear to be the most cost-effective topology for generating reaction force.

However, there are some conditions where the vertical asymmetry generated by the open conic might be desirable. Specifically, some WECs employ a compliant connection between float and heave plate [23], which may benefit from vertical asymmetry to maintain tether tension. Fig. 3.5 shows that conic topologies generate hydrodynamic asymmetry, and enclosing the conic reduces this asymmetry. This asymmetry generally increases with KC, however, we note that asymmetry is negligible for $KC < 1$ and even the 15% difference at $KC = 4$ is not a strikingly asymmetric force profile. This is largely due to symmetric fluid inertia forces, which constitutes the majority of the fluid reaction force (see Chapter 2). Consequently, for WEC developers seeking force asymmetry, drag-dominated topologies are more appropriate, though these designs (e.g., porous plates), produce lower fluid reaction forces than solid structures [32].

Further, when modelling WECs using conventional dynamic-modelling tools that utilize

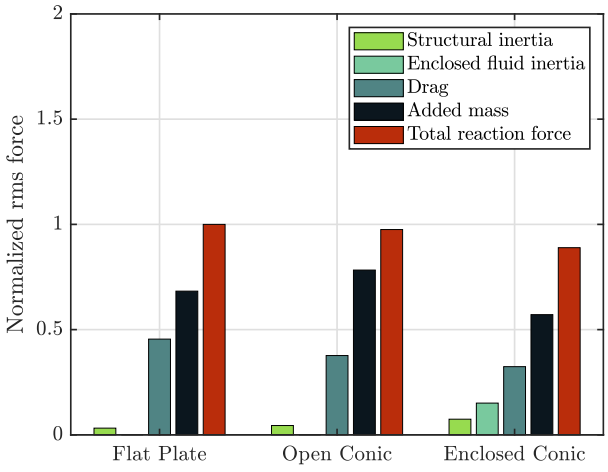

(a)

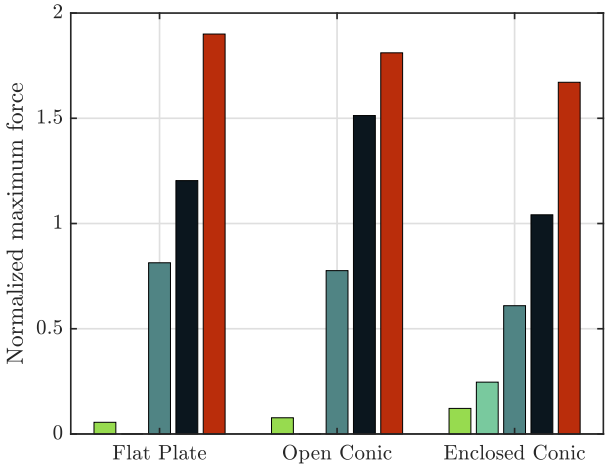

(b)

Figure 3.7: Breakdown of (a) normalized rms and (b) maximum reaction forces for each topology at $KC = 3$, $T = 3$ s. Each bar is normalized by the rms total reaction force for the flat plate.

phase-invariant coefficients, the limits of a phase-invariant Morison equation shown in Fig. 3.4 should be considered. These tools may accurately predict peak forces for $KC < 1$, but at high KC (i.e., more energetic seas), may err by 20 to 25% (Fig. 3.7b). Though a phase-dependent Morison decomposition reduces this error, the method is not without its limitations, as discussed in the next section.

3.4.3 Limits of the phase-dependent Morison decomposition

From the preceding discussion, the hydrodynamic contributions to the fluid force asymmetry shown in Fig. 3.5 would appear straightforward to interpret. However, more complicated hydrodynamic behavior appears when we explore the asymmetry in drag and added mass forces through the phase-dependent Morison decomposition. For this calculation, we apply Eq. 3.4 to phase-dependent F_d (as calculated from $C_d(\theta)$) and F_{fi} (calculated from $C_a(\theta)$ and $F_{i,\text{enclosed}}$). Comparing the magnitude of these forces between the upstroke and downstroke yields an estimate of vertical asymmetry for drag ($F_{d,\text{va}}$) and fluid inertia ($F_{fi,\text{va}}$). As before, a ratio greater than 1 represents higher rms force during the upstroke than the downstroke.

As shown in Fig. 3.8, for $KC > 2$, drag and fluid inertia forces have relatively low vertical asymmetry for the flat plate. The same is generally true for $KC < 1$. However, in the intermediate range ($1 < KC < 2$), the behavior is more complex. While the flat plate has low fluid force asymmetry in this range, the drag force asymmetry is considerable and fluid inertia force asymmetry is also observed. For the open conic, we observe a similar departure from the general trend in this region. For the enclosed conic, drag and inertia forces remain relatively symmetric across all KC.

To understand if these asymmetries and discontinuities, particularly for the flat plate, were an experimental artifact, we repeated the flat plate trials starting from the apex of its oscillation (i.e., $\theta = 0.5$). As shown in Fig. 3.8c and 3.8d, this produced an asymmetry in drag and inertia that almost perfectly mirrored the original experiments where motion originated from the minimum oscillation position (i.e., $\theta = 0$). To investigate the source of this behavior, we focus on a representative experiment with the flat plate, $KC = 1.5$, $T = 2$

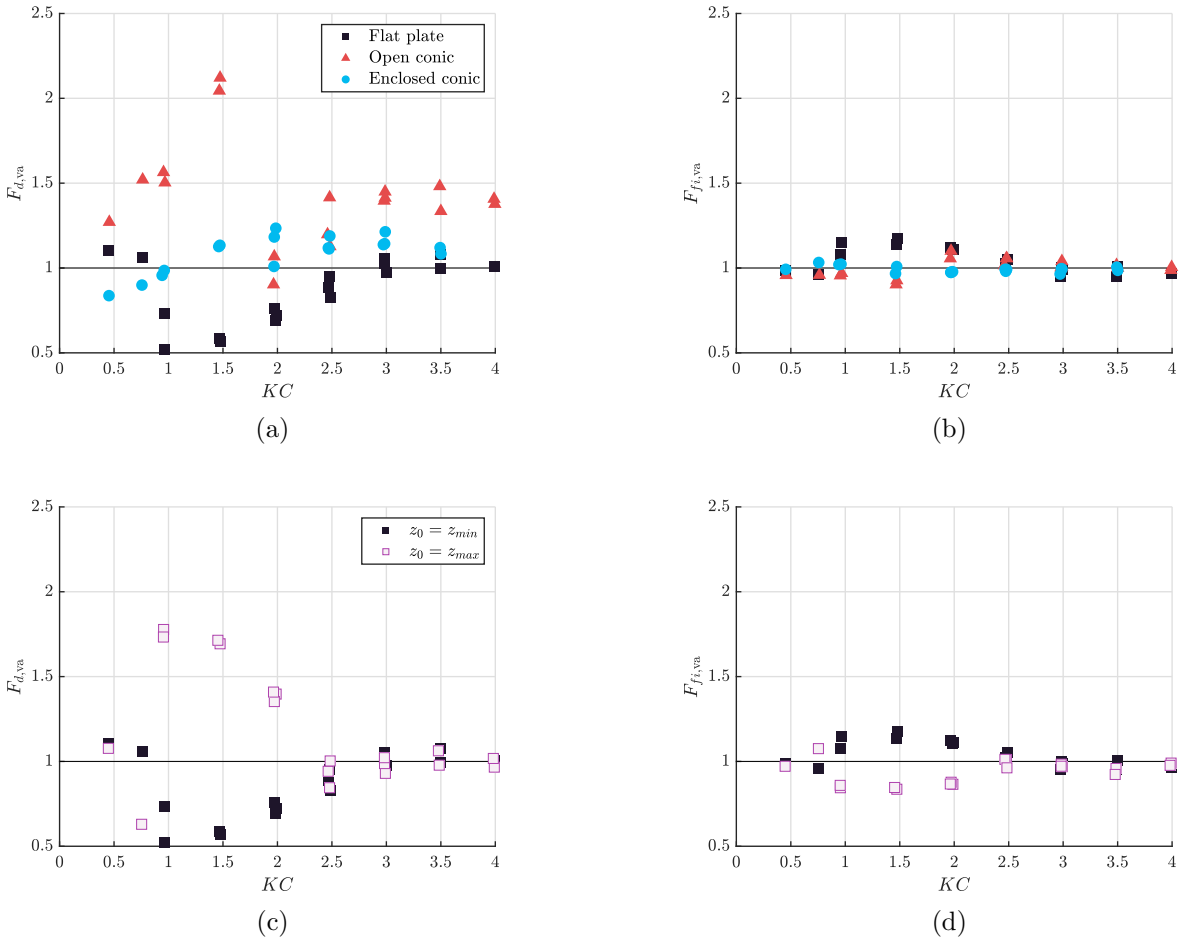

Figure 3.8: Vertical asymmetry in the estimated (a) drag ($F_{d,\mathrm{va}}$) and (b) fluid inertia ($F_{fi,\mathrm{va}}$) force for each topology. The flat plate asymmetry is additionally shown for the two experimental starting conditions - initiation at the bottom and top of the oscillation - for drag (c) and fluid inertia (d). A ratio of 1, denoted by the horizontal line on each panel, represents vertically symmetric forces.

s, and compare the differences in the phase-dependent Morison decompositions to differences in visualized flow around the plate. The hydrodynamic asymmetry is clearly apparent in flow visualization, shown in Fig. 3.9a for the downstroke ($0.5 < \theta < 1$) of two tests with identical oscillation parameters (KC = 1.5, T = 2 s) but different initial positions. The left half of the phase-average image corresponds to $z(t = 0) = z_0 = z_{min}$, and the right to $z_0 = z_{max}$. The four image sequence shows a horizontal slice of the flow, and plate locations correlating to each image are highlighted by the vertical dashed grey lines in Fig. 3.9b-e. Fig. 3.9 shows a distinct correlation between vortex behavior and initial plate position. In particular, at $\theta = 0.67$, the vortex is attached to the plate if $z_0 = z_{min}$, while a vortex is detaching from the plate if $z_0 = z_{max}$. The measured fluid forces also differ between the two cases at this phase, as shown in Fig. 3.9c. Similarly, at $\theta = 0.83$ the detached vortex for $z_0 = z_{max}$ has moved away from the plate, and a new vortex has formed, while the fluid forces for both cases are similar (Fig. 3.9c). The similarity between observed flow structure and measured fluid force are also seen at $\theta = 0.5$ and $\theta = 1$.

Despite similar fluid force extremes, these extreme forces occur at different phases for the two initial conditions shown in Fig. 3.9c. When $z_0 = z_{min}$, more than half the oscillation passes between the force maximum at $\theta \sim 0.1$ and the minimum at $\theta \sim 0.7$ while less than half an oscillation is required to return to the maximum. Because upstroke and downstroke are defined by plate position, not the direction of the fluid force, this distorts the calculated asymmetry in the forces between upstroke and downstroke. Further, as a result of this phase shift, the Morison decomposition allocates more of the fluid force to drag during the downstroke when $z_0 = z_{min}$, and vice versa. This produces the apparent asymmetry in drag and fluid inertia (which are calculated using the Morison equation), despite the limited asymmetry in fluid reaction force (which is derived directly from measurements).

In summary, though geometrically symmetric, a phase-dependent Morison decomposition of flat plate hydrodynamic forces may suggest high drag and added mass asymmetry for some KC. This behavior depends on the initial conditions for oscillation. While the magnitude of the peak reaction force is independent of initial condition, the phase shift in peak reaction

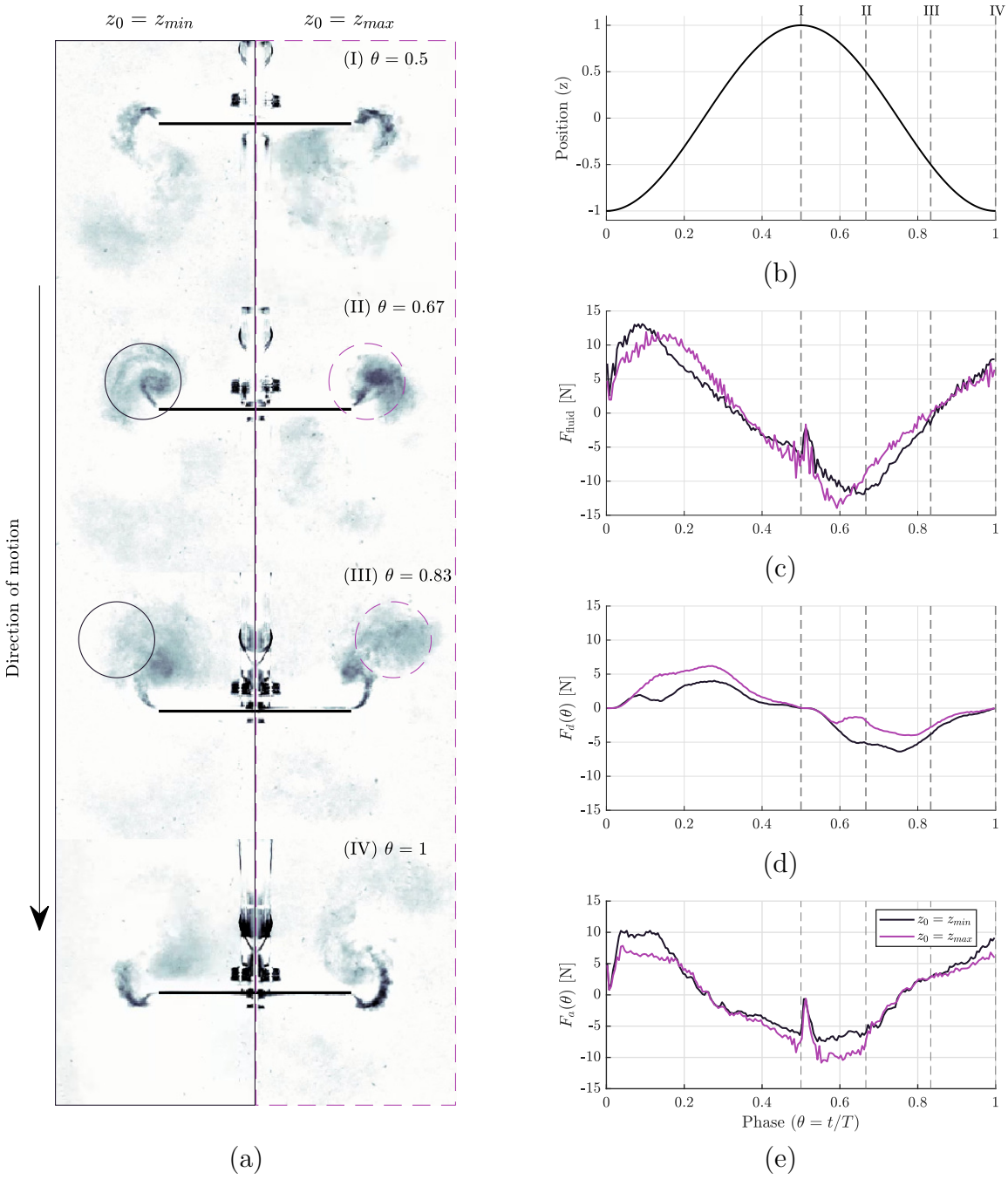

Figure 3.9: (a) Visualization of flow structures near the flat plate oscillating with $KC = 1.5$, $T = 2$ s when the initial condition is $z_0 = z_{min}$ (left), and $z_0 = z_{max}$ (right). (b) Position of the plate relative to phase, and a comparison of the (c) fluid force, (d) drag force, and (e) added mass force for each starting condition. Vertical dashed lines correspond to each snapshot shown in (a).

force produces apparent asymmetries when a Morison decomposition is employed. The differences in the phase of fluid reaction force are correlated with visualized vortex dynamics, suggesting potentially significant links between vortex behavior and hydrodynamic force for an oscillating flat plate.

3.5 Conclusions

We test three heave plate topologies to characterize the role of three-dimensional structure and enclosed fluid on the reaction force generated during oscillation. We show that a flat hexagonal plate generates more fluid force than open or closed hexagonal conics. Additionally, we show that enclosing a hexagonal conic reduces the fluid force generated by the structure.

Phase-dependent analysis of the fluid forces are used to assess the asymmetry between upstroke and downstroke for these topologies. First, the asymmetric topologies are shown to produce asymmetric fluid forces, with a 5 - 10% difference in rms fluid force at low KC, and a maximum of a 15% difference in rms fluid force at $KC = 4$ for the open conic plate. Overall, these non-porous topologies produce limited force asymmetry because they are inertia-dominated and inertial forces are generally symmetric between upstroke and downstroke. Finally, we show that phase-dependent analysis can produce unexpected results for flat plate topologies when $KC = 1 - 2$, suggesting asymmetric drag and added mass for a symmetric flat plate. This is an artifact of how drag and inertia are partitioned by the Morison equation, but caused by real hydrodynamics that are correlated with vortex behavior lock-in and depend on initial plate position.

Chapter 4

EFFECT OF HEAVE PLATE HYDRODYNAMIC FORCE PARAMETERIZATION ON A TWO-BODY WAVE ENERGY CONVERTER

This chapter incorporates the heave plate hydrodynamic parameterizations from Chapters 2 and 3 into two WEC models, both validated against field data. This work is in preparation for submission to the *Journal of Ocean Engineering and Marine Energy*, and information covered in prior chapters has been removed to avoid repetition.

4.1 Introduction

As shown in Chapter 2, KC-dependent, phase-invariant coefficients of drag and added mass ($C_d(KC)$, $C_a(KC)$) accurately represent time-average hydrodynamic forces when $KC < 1$, but may underestimate peak forces by up to 25% at higher KC. That work also showed that coefficients varying in both KC and phase (defined as nondimensional time relative to the minimum oscillation position, $\theta = t/T$) accurately represent $F_h(\theta)$ over a range of KC ($0 < KC < 4$). However, given that heave plate hydrodynamics are just one component of the force balance on a WEC, the benefit of higher-fidelity representations of these forces on aggregate characteristics, such as WEC power output, have not been established. This is, in part, because dynamical models used to simulate WECs (e.g., Proteus DS [7], WEC-Sim [37]) do not support phase-varying coefficients and, in practice, coefficients for a single, representative sea state are often employed. Computational fluid dynamic (CFD) models face no such limitations, as the hydrodynamic forces evolve from the governing equations, but such models can be less accurate than dynamical models, despite their higher computational cost [23]. Regardless of the modeling approach employed, it is important to benchmark

model performance against field data, which are relatively limited.

Consequently, our objective is to determine the significance of time-resolved heave plate hydrodynamics for WEC dynamical simulations. Because most dynamical models cannot accommodate such a parameterization, we employ an analytical model, first verifying its performance against field data, then exploring how increasing the fidelity of heave plate hydrodynamics translates to changes in predicted WEC performance.

4.2 Methods

Drawing on experimental measurements of heave plate reaction forces, we evaluate the impact of three hydrodynamic force parameterizations on WEC performance predicted by an analytical model and, from this, draw conclusions about the significance of these parameterizations for dynamical modeling. The WEC used in our study is a two-body point absorber, called the Wave Energy Buoy that Self-deploys (WEBS). Field data from an instrumented prototype are used to validate a dynamical model, constructed in Proteus DS (DSA, Ltd.) [7], and an analytical model implemented in MATLAB. The dynamical model is used to establish the validity of several simplifications required for analytical modeling.

4.2.1 Heave plate hydrodynamics

As establish in Chapter 2, there are three parameterizations of varying fidelity that could describe the hydrodynamic forces acting on a heave plate. First, across the full matrix of regular sea states, we could represent the hydrodynamics using a single coefficient of drag (C_d) and added mass (C_a), defined for a reference sea state. This is a relatively low-fidelity representation as it will accurately reflect the time-average hydrodynamic forces for sea states near the reference, with errors increasing for sea states further from the reference. Second, we could assign coefficients of drag and added mass based on the KC number experienced by the heave plate ($C_d(KC)$ and $C_a(KC)$). This is a mid-fidelity approximation, which accurately represents hydrodynamic force for $KC < 1$, but has been shown to under predict peak forces for $KC > 1$. Third, for each sea state, we could employ phase-varying coefficients of drag

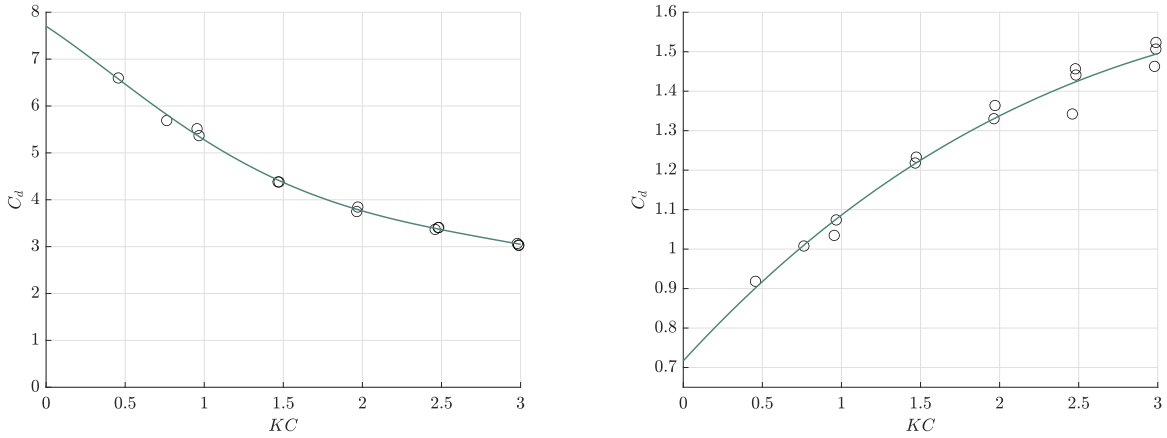

(a) (b)

Figure 4.1: Coefficients of (a) drag and (b) added mass, plotted against KC from experiments Chapter 2, with the best fit equations used to estimate $C_d(KC)$ and $C_a(KC)$. The scatter is a consequence of a secondary dependence on non-dimensional oscillation period. For (a), the approximate lines of fit are $C_d = 7.70 - 2.22KC - 0.90KC^2 + 0.93KC^3 - 0.26KC^4 + 0.02KC^5$ and $C_a = 0.72 + 0.44KC - 0.07KC^2$.

and added mass based on the KC number experienced by the heave plate ($C_d(KC, \theta)$ and $C_a(KC, \theta)$. This is the highest-fidelity representation we could employ, as it captures time-resolved hydrodynamics for all sea states under consideration. All three representations can be implemented in the analytical model, while only the low- and mid-fidelity representations can be implemented in the dynamical model.

Hydrodynamic coefficients are based on prior results (Chapter 2) which experimentally evaluated the hydrodynamic forces acting on a hexagonal conic heave plate with a geometry identical to WEBS, but scaled to $1/10^{\text{th}}$ the size. Fig. 4.1 shows these experimental values with a best fit representation of the coefficients as a function of KC. The dynamical and analytical models predict heave plate motion between $KC = 0.5$ and $KC = 3$ for the sea states considered. For the low-fidelity parameterization, we choose a single value of C_d and C_a based on the central sea state in our matrix of modeled regular waves ($H = 1.2$ m, $T = 10$ s). For the mid-fidelity parameterization, we begin by selecting $C_d(KC)$ and $C_a(KC)$ from

the best fit equations (Fig. 4.1) using heave plate KC values from the low-fidelity model at the same sea state. We then iterate, calculating new $C_d(KC)$ and $C_a(KC)$ values from the actual heave plate KC until differences between iterations are less than 0.1%. For all sea states, the model converged after three iterations.

For high-fidelity, KC- and phase-dependent coefficients ($C_d(KC, \theta)$ and $C_a(KC, \theta)$), we draw upon additional data from Chapter 2. This consists of time series of $C_d(\theta)$ and $C_a(\theta)$ at discrete KC values. These curves are interpolated across KC to create a surface in KC - θ - C_d/C_a space, as shown in Fig. 4.2a and 4.2b that can be queried for any KC and θ. As with the mid-fidelity representation, we employ an iterative solution, which also converges to within 0.1% in three iterations. For all cases, we neglect the first full oscillation, which removes data that occurs before quasi-equilibrium.

4.2.2 WEBS overview

As shown in Fig. 4.3, WEBS is a two-body point absorber with a compliant tether connecting the surface body to a submerged, asymmetric heave plate. The surface body consists of three connected cylinders. The central cylinder, or nacelle, houses a gearbox and generators, remains fully submerged throughout deployment, and is rigidly attached to the aft float. The fore float is free to rotate about the nacelle, and both fore and aft floats are positively buoyant. As the floats heave in response to surface waves, this motion is resisted by the heave plate, producing a change in the relative angle between the surface floats. This rotation drives the generator and allows the WEC to produce electricity. The floats are 3 meters long and mounted 1.2 meters from the nacelle, center to center. The heave plate is suspended roughly 60 meters beneath the nacelle, and measures about 2.5 meters across. Complete specifications for WEBS, which was developed by UW's Applied Physics Laboratory and CPower (Corvallis, OR) are described Appendix A.1.

WEBS was deployed as a freely drifting WEC on the Pacific Ocean in 2016. The conditions during the test were relatively calm, with a 9.66 second peak period and 1.33 m significant wave height, measured by a SWIFT [34] that was deployed alongside WEBS. Rel-

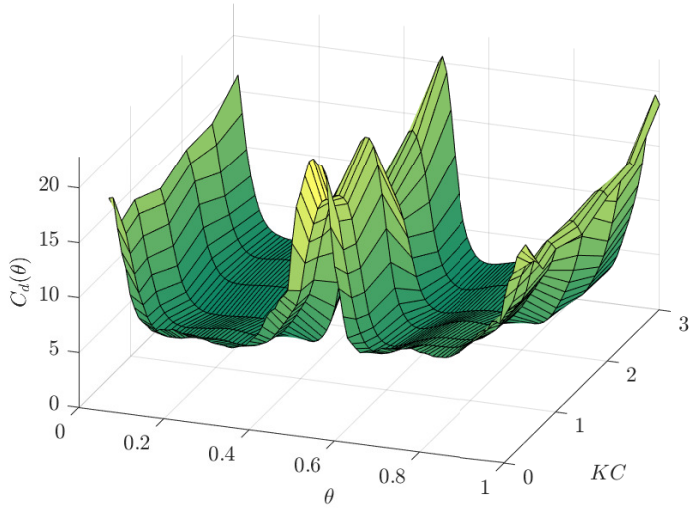

(a)

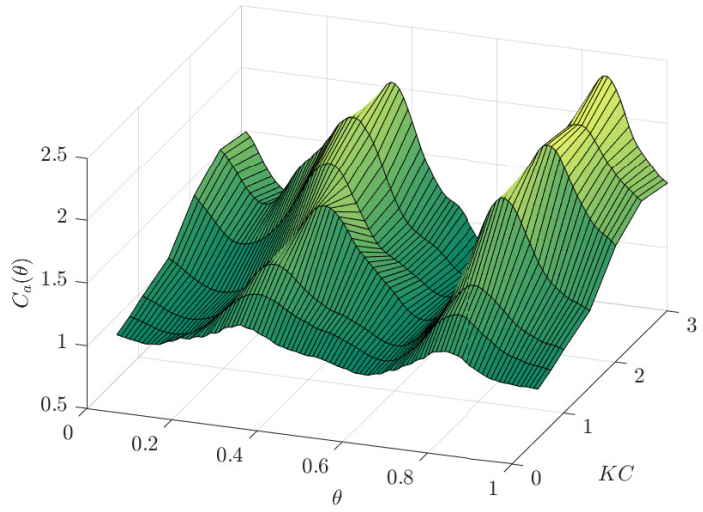

(b)

Figure 4.2: (a) Coefficient of drag and (b) coefficient of added mass in KC - θ space, from experiments presented in Chapter 2

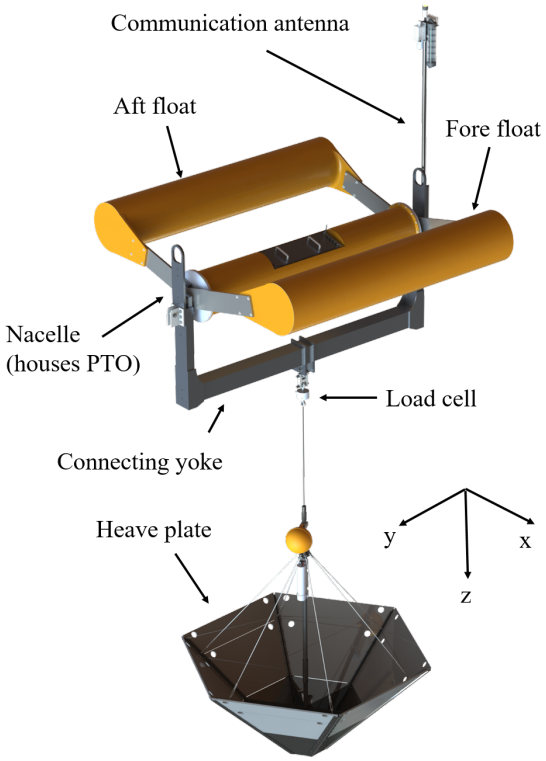

Figure 4.3: Wave energy buoy that self-deploys (WEBS). Note that the tether length is not to scale.

evant data collected throughout the deployment includes generator encoder position, tether tension, and heave plate pressure.

4.2.3 WEBS models

We employ two time-domain models to predict the response of WEBS across sea states: an analytical model implemented in MATLAB, and a dynamical model implemented in a commercial code, Proteus DS [7]. We identify the main sources of differences between models using a simplified dynamical model, which approximates the analytical model. In this section, we discuss these models and their assumptions.

WEC geometry is identical between the models. We neglect all radiation and excitation forces in both models and assume that nacelle and heave plate motion are restricted to heave. The PTO dynamics are parameterized as a spring-damper system with constant spring and damping coefficients. Electrical power output is calculated from PTO velocity and incorporates estimates for generator efficiency (Appendix A.1).

The two models differ in three main ways, as summarized in Table 4.1. First, the analytical model makes the assumption that the WEC dynamics are driven solely by changes in buoyancy due to variable submergence of the fore and aft floats. In contrast, the dynamical model also includes drag, added mass, and Froude-Krylov forces on the floats and nacelle. Second, the analytical model assumes a perfectly rigid connection between the heave plate and nacelle, while the dynamical model represents the tether as a cable with 20 elements. Third, the analytical model assumes that the heave plate does not experience any wave orbital motion, while the dynamical model explicitly calculates the wave-induced velocities acting on the heave plate.

For validation against field data, we force these models with an irregular wave field with the same statistics as the field test. The dynamical model produces a time series of surface elevation that follows a Pierson-Moskowitz spectrum with $H_s = 1.33$ m and $T_p = 9.66$ s, and this time series is subsequently used as input for the analytical model. A simulation with 695 s duration was chosen so as to utilize one full 'repeat period' [7]. Additional

Table 4.1: Main differences between dynamical and analytical model

Parameter	Model	
	Dynamical	Analytical
Float forces	Buoyancy Gravity Drag Added mass Froude-Krylov	Buoyancy Gravity
Tether	20 element cable	Rigid connection
Heave plate depth	61 m	∞ (below orbital motion)

details of the dynamical model are provided in Appendix A.2. We represent heave plate hydrodynamics using a single coefficient of drag and added mass, chosen using the peak wave height of 1.33 m. Assuming the heave plate experiences motion similar to the wave height, we predict $KC \approx 1.5$, yielding $C_d = 4.4$ and $C_a = 1.2$. This is analogous to a mid-fidelity parameterization, but the irregular waves yield instantaneous heave plate motions with both higher and lower KC values.

The dynamical model is then used to verify the analytical model for a range of regular waves. We analyze model outputs for waves with periods (T) from 7 - 13 s, and wave heights (H) of 0.5 - 1.9 meters. For larger wave heights and smaller periods, slack loading occurs in the tether and dominates the WEC response. Since this cannot be represented by the analytical model, we present results only for regular wave cases without slack loading. The source of observed differences between the dynamical and analytical models is explored with a simplified dynamical model that incorporates the same assumptions as the analytical model. While a few minor difference remain, as discussed in Sec. 4.2.3, the simplified dynamical model is as similar to the analytical model as we can control for within the framework of the commercial software.

The analytical model solves the equations of motion governing WEBS, namely linear motion in z-direction and rotational motion about the nacelle. These are presented in Appendix A.3. The governing equations are solved using MATLAB's ordinary differential equation

solver ODE45. Sea surface elevation is the model input and WEBS motion is the model output.

4.2.4 WEC performance metrics

We use three metrics to assess the performance of WEBS: heave plate motion, tether tension, and electrical power output from the generator. As we will show, heave plate KC, which is a measure of the range of heave plate motion for a given sea state, is critical to the selection of accurate hydrodynamic coefficients. Tether tension is the reaction force transmitted from the heave plate to the surface body, and we focus on maximum tension in analysis, which is critical for design load calculations on the tether and connection points. Electrical power output is the ultimate measure of WEC suitability for a given application and we focus on time-average power for each sea state. For all models, start-up effects impact the first full wave period, which is discarded prior to analysis.

4.3 Results

4.3.1 Dynamical and analytical model verification in irregular seas

We first compare model results in irregular waves with field data from WEBS. Fig. 4.4 shows that the models produce similar distributions of WEC performance metrics. Heave plate position is represented most accurately, with both models picking up the slight skew in the data and the general shape of the distribution. The differences in tether tension are a consequence of model assumptions. The dynamical model slightly under-predicts the slack loading conditions observed in the field data, likely due to the chain weight that kept the WEBS load cell in slight tension through slack loading conditions, a feature not included in the models. The analytical model is skewed because the approximation of the tether as a rigid member allows for compression. This is reflected in the negative tensile loading data. Power approximations follow the same trends, though the models each have a longer tail than field data, leading to an over-prediction of mean power output. Overall, these results suggest

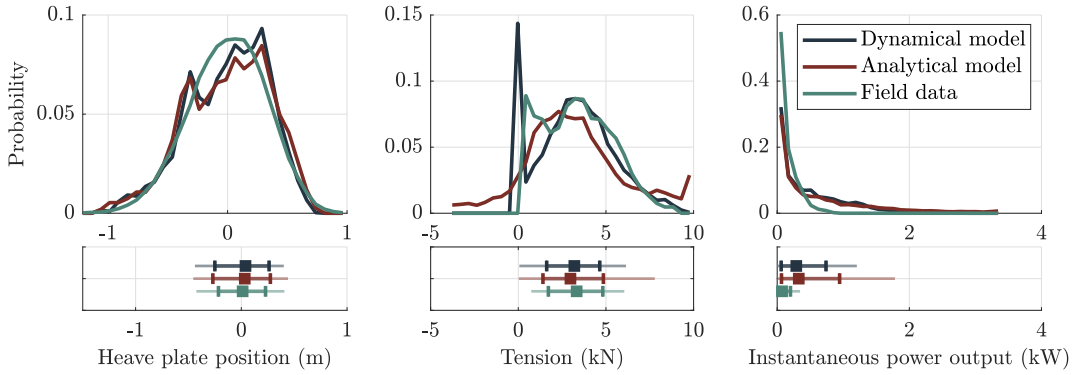

Figure 4.4: Probability distributions of WEC performance metrics for field data with corresponding outputs from the dynamical and analytical model for an irregular sea state with $T_P = 9.66$ s and $H_s = 1.33$ m. Below each distribution is a box plot showing the median value for each dataset (symbols), along with the interquartile range (thick lines) and extent of 10^{th} and 90^{th} percentile values (whiskers).

that the dynamical and analytical model are both reasonable approximations of WEBS at this sea state.

4.3.2 Dynamical and analytical model comparison in regular waves

With confidence that the models are consistent with WEBS performance, we estimate the accuracy of the analytical model by comparing it to the dynamical model across a range of regular sea states. At the center of this range is a wave with a 10 s period and 1.2 m wave height. As shown in Fig. 4.5, predicted heave plate motion is similar between the dynamical and analytical model, which estimate a heave plate KC of 1.58 and 1.64, respectively. Quantitative agreement is poorer for tether tension and power output. Given that the simplified dynamical model, which uses the same assumptions as the analytical model, (Table 4.1) has better agreement, this suggests that the differences are primarily explained by the differences in assumptions. However, we note that despite the differences in amplitude and phase, the dynamical and analytical models predict similar average values (e.g., electrical power outputs of 0.37 kW and 0.41 kW, respectively).

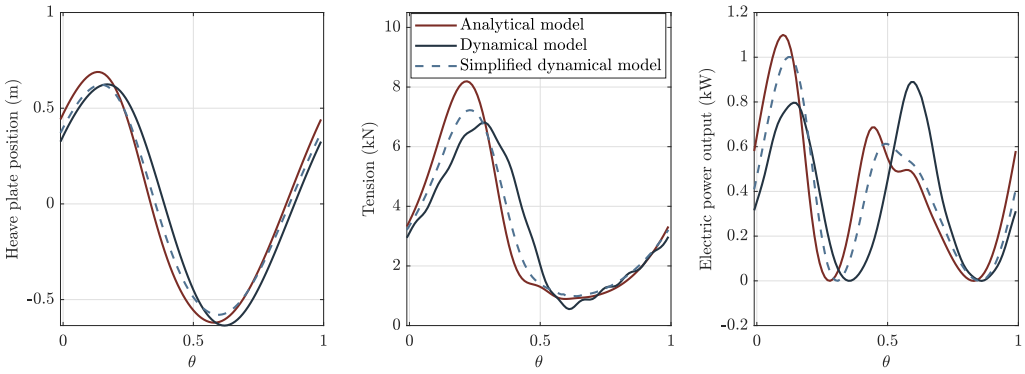

Figure 4.5: Comparison of a representative time series between the analytical, dynamical, and simplified dynamical models for a regular wave with $H = 1.2$ m and $T = 10$ s, for heave plate position, tether tension, and electrical output.

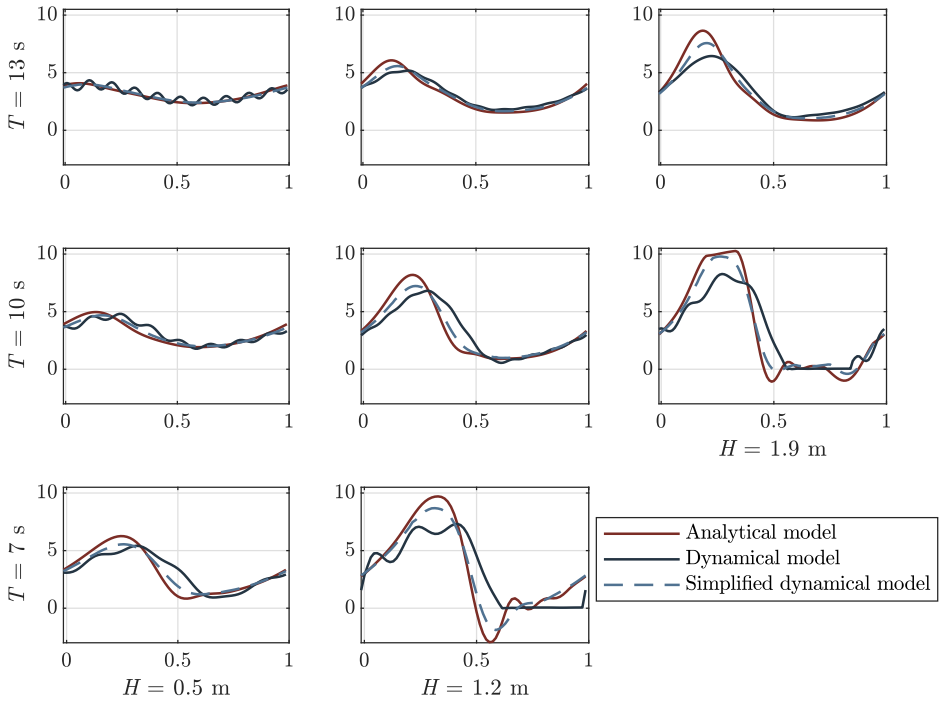

Figure 4.6: Comparison of tether tension time series (kN) predicted by the analytical, dynamical, and simplified dynamical models for waves with periods of 7, 10 and 13 s, and heights of 0.5, 1.2, and 1.9 m.

A similar comparison is shown for tether tension over the full range of sea states is shown in Fig. 4.6. As expected, tether tension depends on H and T, and we see greater disagreement for shorter periods and larger waves. This is a consequence of slack loading, which is poorly represented by a rigid heave plate connection. As such, cases with slack loading are excluded from further comparisons. Outside of this region, the analytical model shows acceptable quantitative agreement with the dynamical model, with differences decreasing when the dynamical model uses the same assumptions as the analytical model.

4.3.3 Effect of KC-dependent coefficients

Given the demonstrated accuracy of the analytical model, we turn to comparisons between low- and mid-fidelity coefficients (i.e., $C_{d,a}$ vs. $C_{d,a}(KC)$). Fig. 4.7a shows a small change in heave plate motion between these parameterizations. Predictably, error is minimized at the center of the heat map, which corresponds to the reference case for the single coefficient parameterization. The difference between $C_{d,a}$ and $C_{d,a}(KC)$ increases as wave height diverges from $H = 0.9$. The use of KC-dependent coefficients increases predicted heave plate motion by up to 9% at a wave height of 1.9 m, and decreases predicted motion by about 6% for a wave height of 0.5 m. Maximum tether tension is predicted with 10% lower values at $H =$ 0.5 m and 15% higher at $H = 1.9$ m for KC-dependent coefficients (Fig. 4.7b. We see the largest impact on average power prediction (Fig. 4.7c), where differences between mid- and low-fidelity coefficients range from -30% to +30%.

4.3.4 Effect of KC- and phase-dependent coefficients

High-fidelity coefficients dependent on both KC and phase can accurately represent time-dependent heave plate hydrodynamics from $KC = 0 - 4$ (as shown in Chapter 2). Shown in Fig. 4.8a, this parameterization ($C_d(KC, \theta)$, $C_a(KC, \theta)$) yields almost identical heave plate motion as the mid-fidelity parameterization ($C_d(KC)$, $C_a(KC)$), with less than 2% difference for all cases. While the impact on tension and power is larger, overall differences remain relatively small. For maximum tether tension (Fig. 4.8b), phase-dependent hydrodynamics

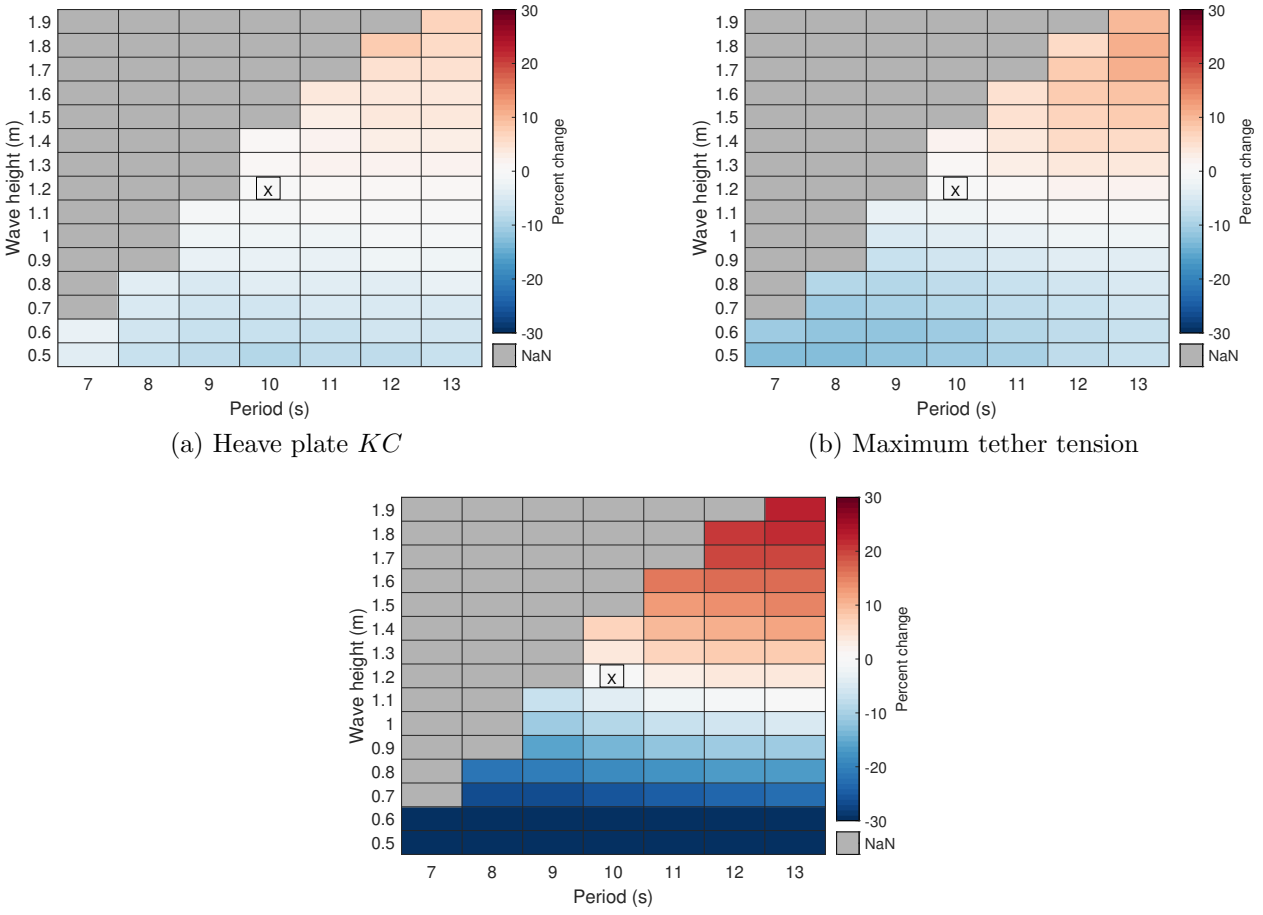

(a) Heave plate KC

(b) Maximum tether tension

(c) Average electrical power output

Figure 4.7: Heat map showing the percent change moving from a model with low-fidelity coefficients to mid-fidelity coefficients for (a) heave plate KC, (b) maximum tension and (c) average electrical power when comparing. The 'X' denotes the case in which coefficients are identical between models. Sea states with tether compression are shown in grey as NaN.

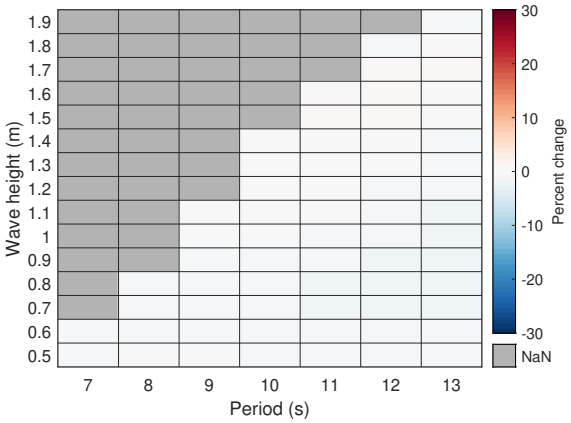

(a) Heave plate KC

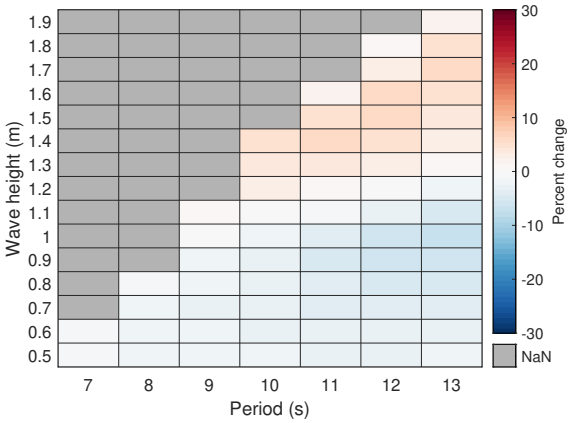

(b) Maximum tether tension

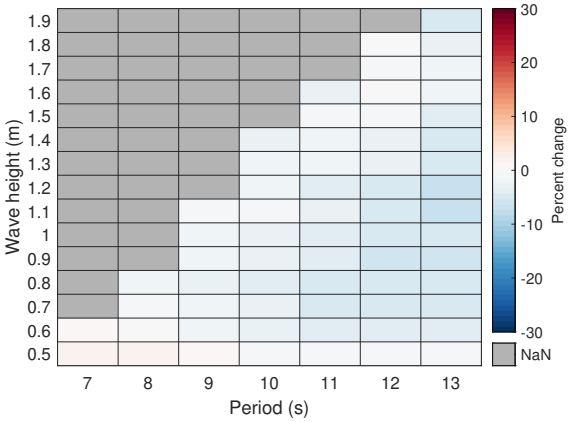

(c) Average electrical power output

Figure 4.8: Heat map showing the percent change moving from a model with mid-fidelity coefficients to high-fidelity coefficients for (a) heave plate KC, (b) maximum tension and (c) average electrical power. Sea states with tether compression are shown in grey as NaN.

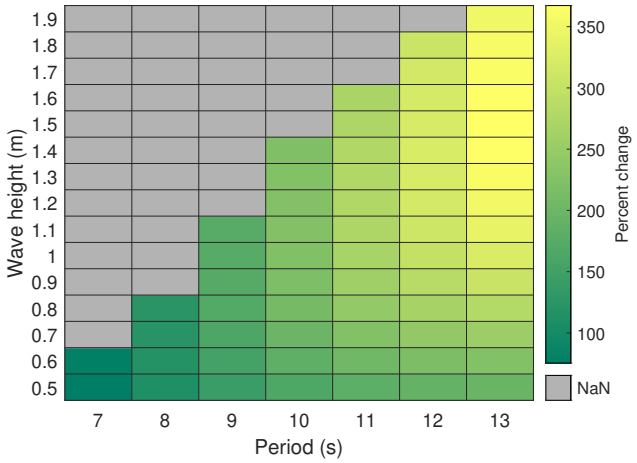

Figure 4.9: Percent change in average electrical power output that occurs when using KC-dependent coefficients of drag and added mass compared to a model using coefficients of added mass from BEM and drag from theory.

yields peak differences of -6% to +6%. Average power output is predicted to be slightly lower for nearly every wave case (Fig. 4.8c), but are, at most 7% lower.

4.4 Discussion

4.4.1 Impact of KC-dependent hydrodynamics

Predictions of heave plate motion, tether tension, and electrical power output change based on the heave plate hydrodynamic parameterization. For the low-fidelity model, as H and T diverge from the reference case at $H = 0.9$ m, $T = 12$ s, $C_d(KC)$ and $C_a(KC)$ similarly diverge from their reference values (e.g., for larger wave heights, $C_d(KC) < C_d$ and $C_a(KC) > C_a$). Since heave plate hydrodynamic force is dominated by added mass force (see Chapter 2), higher added mass coefficients predictably yield higher maximum tension values and average power outputs. Less obviously, this also correlates to larger heave plate motions due to higher heave plate inertia and lower drag. Because heave plate hydrodynamics are modeled solely as a function of KC, these changes are primarily dependent on wave height, rather than period.

If experimental data are not available to estimate hydrodynamic coefficients, WEC models may employ a Boundary Element Method (BEM) to calculate hydrodynamics for a given geometry. For the conic heave plate used in WEBS, the BEM code NEMOH [1] predicts an added mass coefficient of 0.6, which is less than the prediction from experimentally-derived values for $KC = 0$ (Fig. 4.1). If we pair this BEM estimate of added mass with a theoretical drag coefficient of about 1.5 for a cone (averaged between the two orientations, [11]), electrical power estimates differ from those of our low-fidelity representation by 200-300%, as shown in Fig. 4.9. This emphasizes the importance of accurate, geometry-specific hydrodynamic coefficients for dynamical modeling, particularly for added mass.

4.4.2 Impact of phase- and KC-dependent hydrodynamics

The change in predicted WEC performance that occurs from low- to mid-fidelity parameterizations is substantial. However, the additional complexity associated with moving from mid- to high-fidelity parameterizations does not lead to substantial changes in WEC performance. High-fidelity parameterizations predict similar values for heave plate KC, maximum tether tension, and average power output relative to mid-fidelity prameterizations. While average power output uniformly decreases when high-fidelity paramweterizations are employed, the change ($< 7\%$) is inconsequential compared to other model uncertainties (i.e., difference between model outputs and field data). Overall, implementing phase-varying hydrodynamics adds significant complexity to the model, while producing limited benefits for simulation accuracy.

4.4.3 Limitations

A few caveats apply to these results. First, we have only considered the effects of hydrodynamic parameterizations on a single two-body point absorber for a relatively narrow range of significant wave heights. This limitation is a consequence of the field data available to validate the models and the inability of the analytical model to represent slack loading in the tether, which becomes increasingly likely for larger wave heights and shorter wave pe-

riods. While the first consideration can only be addressed by broader availability of WEC field data, the accuracy of mid-fidelity parameterization suggests that a wider range of sea states could be effectively explored by with a dynamical model employing KC-dependent coefficients (i.e., the unquantified quadrants of Fig. 4.7 and 4.8 could be populated with a dynamical model). However, given the poor accuracy obtained by a low-fidelity parameterization for sea states that do not produce a slack loading, this would not fundamentally affect our recommendation to employ mid-fidelity hydrodynamic parameterizations.

4.5 Conclusion

We have shown that an analytical model of WEBS provides a realistic representation of the WEC behavior in irregular seas. The analytical model also shows good quantitative agreement to a dynamical model with additional physics in regular waves, provided that no slack loading occurs in the tether connecting the nacelle and heave plate. As such, the analytical model is suitable to evaluate the effect of low-, mid-, and high-fidelity parameterizations of heave plate hydrodynamics on WEC performance.

We find that a mid-fidelity parameterization, in which hydrodynamic coefficients vary only with heave plate KC, provides significant accuracy improvements in modeling WEC performance, with up to 30% improvement in estimates for electrical power output relative to a low-fidelity parameterization assuming a constant KC for all sea states. Further, even the low-fidelity model significantly out-performs a simulation relying on estimates of drag from theory and added mass from BEM. Finally, we show that a high-fidelity parameterization, in which hydrodynamic coefficients vary in both KC and phase, provides limited benefit to model accuracy. We thus conclude that dynamical WEC models should employ experimental coefficients that vary with KC, but should not attempt to incorporate phase variation.

Chapter 5

CONCLUSIONS AND FUTURE WORK

5.1 Conclusions

Through this work, we characterize the hydrodynamics of heave plates for two-body, point absorber wave energy converters using a Morison decomposition and incorporate these hydrodynamics into an analytical model, which we verify against field data. This provides a more in-depth analysis of scaling for phase-varying hydrodynamics than any prior work. The effect of enclosed fluid on the dynamics of an oscillating body has also not been well-studied, and the additional observations of hydrodynamic asymmetry correlated with vortex behavior for a flat oscillating plate is valuable information for design of future experimental campaigns. Finally, this work represents one of few public efforts to validate dynamical and analytical models of a two-body WEC against a field deployment. This provides guidance to future WEC researchers to use empirical, KC-dependent coefficients in their simulations and not to rely on canonical or BEM-derived coefficients as these may only be order of magnitude approximations.

In Chapter 2, we characterize the hydrodynamics of an asymmetric heave plate at three scales. This work shows that coefficients of drag and added mass scale with KC for an asymmetric heave plate. The accuracy of the phase-invariant Morison equation decomposition decreases as KC increases. Phase-dependent decomposition of the Morison equation, which accurately reconstructs heave plate hydrodynamics for all KC, shows that intra-cycle added mass variability increases with KC and is primarily responsible for the increased reconstruction error using phase-invariant coefficients at $KC > 1$. Further, flow visualization shows vortex development and shedding that is correlated with trends in phase-dependent added mass.

In Chapter 3, we investigate the role of topology in the reaction force produced by heave plates. To achieve this, we re-test the open hexagonal conic used in Chapter 2, alongside a flat plate with equal planform area, and an assembly of the flat and open conic plates, trapping fluid inside the cavity of the hexagonal conic. The results show that enclosing a hexagonal conic counter-intuitively reduces total reaction force due to a relatively large reduction in hydrodynamic forces. Conversely, we show that a flat plate produces more reaction force than the three-dimensional topologies, but experiences hydrodynamic force asymmetry from $KC = 1 - 2$ in regular oscillation. We determine that this asymmetry appears alongside asymmetric vortex shedding, and that both phenomena are dependent on the starting condition for the test.

Finally, in Chapter 4 we verify dynamical and analytical models for a two-body point absorber WEC with a hexagonal conic heave plate in irregular waves against field data. We further verify the analytical model in regular waves using the dynamical model, showing that, despite many simplifications (neglecting all surface forces aside from buoyancy, rigid heave plate to nacelle connection, infinitely deep heave plate), the analytical model captures most of the relevant physics. We implement three different parameterizations of heave plate hydrodynamics in the analytical model to assess the impact of these parameterizations on modelled WEC response. The results show that the use of mid-fidelity, KC-dependent coefficients provides a 30% change in modelled power output at the edges of our evaluation domain ($H = 0.5 - 1.9$ m, $T = 7 - 13$ s) when compared to a low-fidelity coefficient that is accurate for the center of the domain. Further, the use of high-fidelity, phase- and KC-dependent coefficients yields less than a 5% change when compared to models with mid-fidelity coefficients. Finally, we show that a BEM-derived added mass coefficient leads to power prediction errors in excess of 200%. This informs a recommendation for modellers to use mid-fidelity, KC-dependent heave plate hydrodynamic coefficients, as these represent a balance between the inaccuracy of BEM-derived coefficients or low-fidelity KC-independent coefficients and the complexity of high-fidelity KC- and phase-dependent coefficients.

5.2 Future work

While multiple avenues for future work exist, we wish to highlight two key focus areas. First, most of these results apply to regular waves. Given the irregular nature of real ocean waves, further experimental characterization of heave plate hydrodynamics in irregular waves is a logical next step. This would help assess the accuracy of KC-dependent coefficients when they are applied to models of a WEC in irregular waves. These experiments would involve force measurement during irregular oscillation of a heave plate, and subsequent evaluation of reconstruction error when using KC-dependent coefficients that align with the experimental significant wave height. If this technique shows significant error, additional strategies could be explored to represent irregular wave hydrodynamics in a phase-varying sense.

Additionally, this work could spur further research on optimal heave plate design. With a validated WEC model, iterative modelling efforts would allow for convergence on heave plate hydrodynamic coefficients that maximize power production or regulate maximum tether tension. We have shown that hydrodynamics are important to WEC response, and therefore optimization of those hydrodynamics is key to maximizing power output. Given a range of optimal hydrodynamics, new designs could work towards these ideal coefficients through experimental tests of small-scale heave plates, as demonstrated in Appendix B.

BIBLIOGRAPHY

[1] Aurelien Babarit and Gerard Delhommeau. Theoretical and numerical aspects of the open source BEM solver NEMOH. In *11th European Wave and Tidal Energy Conference*, pages 1 – 12, Nantes, France, 2015.

[2] A. B. Basset. On the motion of a sphere in a viscous fluid. *Philosophical Transactions Royal Society of London A*, 179:43–63, 1888.

[3] Scott J. Beatty, Matt Hall, Bradley J. Buckham, P. Wild, and B. Bocking. Experimental and numerical comparisons of self reacting point absorber wave energy converters in regular waves. *Ocean Engineering*, 104:370–386, 2015.

[4] Ana Bezunartea, Sergio Ruano, Adolfo Maron, Enrique Molinelli Fernández, Francisco Moreno-Burón, Julio Oria-Escudero, José Riós-Tubio, Cristina Soriano-Gomez, Álvaro Valea, Carlos Lopez-Pavon, and Antonio Souto-Iglesias. Scale effects on heave plates for semi-submersible floating offshore wind turbines: case study with a solid plain plate. *Journal of Offshore Mechanics and Arctic Engineering*, pages 1–14, 11 2019. doi: 10.1115/1.4045374.

[5] Adam Brown, Jim Thomson, and Curtis Rusch. Hydrodynamic coefficients of heave plates, with application to wave energy conversion. *IEEE Journal of Oceanic Engineering*, 43(4), October 2018. doi: 10.1109/JOE.2017.2762258.

[6] K. Budal and J. Falnes. A resonant point absorber of ocean-wave power. *Nature*, 256 (5517):478, 1975. ISSN 0028-0836.

[7] DSA. ProteusDS manual. `http://downloads.dsa-ltd.ca/documentation/ProteusDS\%202015\%20Manual.pdf`, July 2018.

[8] Carlos A. Garrido-Mendoza, Krish P. Thiagarajan, Antonio Souto-Iglesias, Benjamin Bouscasse, and Andrea Colagrossi. Numerical investigation of the flow features around heave plates oscillating close to a free surface or seabed. In *33rd International Conference on Ocean, Offshore and Arctic Engineering*, pages 1–11. ASME, 2014. doi: 10.1115/OMAE2014-23818.

[9] Carlos A. Garrido-Mendoza, Krish P. Thiagarajan, Antonio Souto-Iglesias, Andrea Colagrossi, and Benjamin Bouscasse. Computation of flow features and hydrodynamic coefficients around heave plates oscillating near a seabed. *Journal of Fluids and Structures*, 59:406–431, 2015. ISSN 10958622. doi: 10.1016/j.jfluidstructs.2015.10.003.

[10] Kester Gunn and Clym Stock-Williams. Quantifying the global wave power resource. *Renewable Energy*, 44:296 – 304, 2012. ISSN 0960-1481. doi: https://doi.org/10.1016/j.renene.2012.01.101. URL `http://www.sciencedirect.com/science/article/pii/S0960148112001310`.

[11] Sighard F. Hoerner. *Fluid-dynamic drag: practical information on aerodynamic drag and hydrodynamic resistance*. Dr.-Ing. S.F. Hoerner, Midland Park, N.J., 1958.

[12] G. H. Keulegan and L. H. Carpenter. Forces on cylinders and plates in an oscillating fluid. *Journal of Research, National Bureau of Standards*, 60(5), May 1958.

[13] Jinxuan Li, Shuxue Liu, Min Zhao, and Bin Teng. Experimental investigation of the hydrodynamic characteristics of heave plates using forced oscillation. *Ocean Engineering*, 66:82–91, 2013. ISSN 00298018. doi: 10.1016/j.oceaneng.2013.04.012.

[14] Ye Li and Yi-Hsiang Yu. A synthesis of numerical methods for modeling wave energy converter-point absorbers. *Renewable and Sustainable Energy Reviews*, 16(6):4352 – 4364, 2012. ISSN 1364-0321. doi: https://doi.org/10.1016/j.rser.2011.11.008. URL `http://www.sciencedirect.com/science/article/pii/S1364032111005351`.

[15] James Lighthill. Fundamentals concerning wave loading on offshore structures. *Journal of Fluid Mechanics*, 173:667–681, 1986. doi: 10.1017/S0022112086001313.

[16] A. LiVecchi, A. Copping, D. Jenne, A. Gorton, and G. Gill R. Preus, R. Robichaud, R. Green, S. Geerlofs, S. Gore, D. Hume, W. McShane, C. Schmaus, and H. Spence. Powering the Blue Economy; Exploring Opportunities for Marine Renewable Energy in Maritime Markets. Technical report, U.S. Department of Energy, Office of Energy Efficiency and Renewable Energy, Washington, D.C., 2019.

[17] J. S. McNown and G. H. Keulegan. Vortex formation and resistance in periodic motion. *Journal of Engineering Mechanics Division*, 85(1):1–6, 1959.

[18] J. R. Morison, M. P. O'Brien, J. W. Johnson, and S. A. Schaaf. The force exerted by surface waves on piles. *Journal of Petroleum Technology*, 189:149–154, 1950.

[19] T. Mundon, B. Rosenberg, and J. Rij. Reaction body hydrodynamics for a multi-dof point-absorbing wec. In A. Lewis, editor, *Proceedings of the Twelfth European Wave and Tidal Energy Conference*, pages 1– 10, University College Cork, Ireland, Aug 27–Sep 1 2017. EWTEC. ISSN: 2309-1983.

[20] J N Newman. Amplification of waves by submerged plates. In *Proc of 30th IWWWFB*, pages 1–4, Bristol, UK, 2015.

[21] Orcina. OrcaFlex specifications. `https://www.orcina.com/orcaflex/specification/`, 2020. Accessed: 04-16-2020.

[22] B. J. Rosenberg and T. R. Mundon. Numerical and physical modeling of a flexibly-connected two-body wave energy converter. In *Marine Energy Technology Symposium*, pages 1–4, 2016.

[23] B. J. Rosenberg, T. Mundon, Ryan G. Coe, Eliot W. Quon, Chris C. Chartrand, Yi-Hsiang Yu, and Jennifer van Rij. Development of WEC design loads: A comparison

of numerical and experiemental approaches. In *Proceedings of the Thirteenth European Wave and Tidal Energy Conference*, pages 1 – 8, Naples, Italy, Sep 1 – 6 2019. EWTEC.

[24] Curtis Rusch. Wave energy buoy that self-deploys. Technical report, Department of Mechanical Engineering, University of Washington, 2020. URL `https://drive.google.com/file/d/1-YpXIPmTdJisCj2IrDLPseJumUQx4KlX/view`.

[25] Curtis J. Rusch, Tim R. Mundon, Benjamin D. Maurer, and Brian L. Polagye. Hydrodynamics of an asymmetric heave plate for a point absorber wave energy converter. *Ocean Engineering*, 215:107915, 2020. ISSN 0029-8018. doi: https://doi.org/10.1016/j.oceaneng.2020.107915. URL `http://www.sciencedirect.com/science/article/pii/S002980182030874X`.

[26] T. Sarpkaya. Unsteady flows. In J.A. Schets and A.E. Fuhs, editors, *Handbook of Fluid Dynamics and Fluid Machinery*, volume 1, chapter 12, pages 697–732. Wiley, New York, 1996.

[27] T. Sarpkaya. Resistance in unsteady flow: search for an in-line force model. *International Journal of Offshore and Polar Engineering*, 10(4):249–254, 2000.

[28] T. Sarpkaya. On the force decompositisions of Lighthill and Morison. *Journal of Fluids and Structures*, 15:227–233, 2001. doi: 10.1006/jfls.2000.0342.

[29] T. Sarpkaya. A critical review of the intrinsic nature of vortex-induced vibrations. *Journal of Fluids and Structures*, 19:389– 447, 2004. doi: 10.1016/j.jfluidstructs.2004.02.005.

[30] Turgut Sarpkaya and Michael Isaacson. *Mechanics of Wave Forces on Offshore Structures*. Van Nostrand Reinhold Company, New York, N.Y., 1981.

[31] Sir G. G. Stokes. On the effect of internal friction of fluids on the motion of pendulums. *Transactions of the Cambrige Philisophical Society*, IX:8–106, 1851.

[32] Longbin Tao and Daniel Dray. Hydrodynamic performance of solid and porous heave plates. *Ocean Engineering*, 35(10):1006–1014, 2008. ISSN 00298018. doi: 10.1016/j.oceaneng.2008.03.003.

[33] Longbin. Tao and Krish P. Thiagarajan. Low KC flow regimes of oscillating sharp edges. I. vortex shedding observation. *Applied Ocean Research*, 25(1):21–35, 2003. ISSN 01411187. doi: 10.1016/S0141-1187(03)00046-4.

[34] Jim Thomson. Wave breaking dissipation observed with "SWIFT" drifters. *Journal of Atmospheric and Oceanic Technology*, 29(12):1866–1882, 2012. doi: 10.1175/JTECH-D-12-00018.1.

[35] Wamit. WAMIT technical description. `https://www.wamit.com/techdescription.htm`, 2019. Accessed: 03-25-2020.

[36] Zhangping Wei, Billy L. Edge, Robert A. Dalrymple, and Alexis Hérault. Modeling of wave energy converters by gpusph and project chrono. *Ocean Engineering*, 183:332 – 349, 2019. ISSN 0029-8018. doi: https://doi.org/10.1016/j.oceaneng.2019.04.029. URL `http://www.sciencedirect.com/science/article/pii/S0029801818317608`.

[37] Y.-H. Yu, M. Lawson, K. Ruehl, and C. Michelen. Development and demonstration of the WEC-Sim wave energy converter simulation tool. In *Proceedings of the 2nd Marine Energy Technology Symposium*, pages 1–8, Seattle, WA, 2014.

Appendix A

WAVE ENERGY BUOY THAT SELF-DEPLOYS (WEBS)

A.1 WEBS specifications

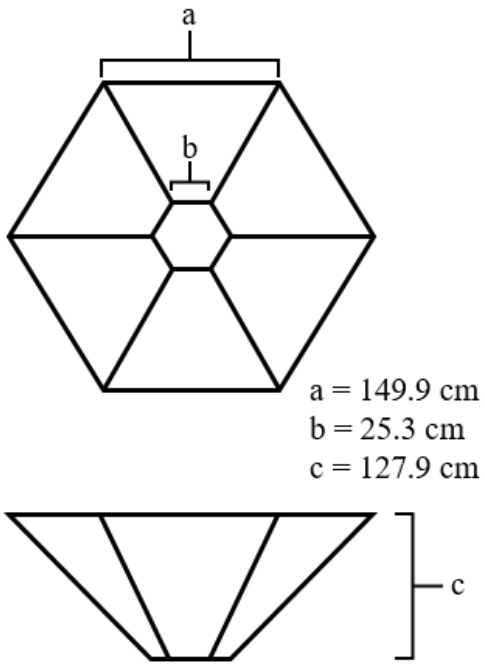

Figure A.1: Design measurements for the WEBS open hexagonal conic heave plate.

Here we show the specifications for WEBS, as presented in [24], which are also used in the dynamical and analytical models. Table A.1 outlines specifications for all critical WEBS components. Table A.2 shows secondary specifications required for numerical simulation. The values listed for center of gravity are for the device in a horizontal position, where the nacelle arm is parallel to the sea surface (i.e., $\phi = 90°$).

Additional detail for the heave plate design is given Fig. A.1. Elongation properties

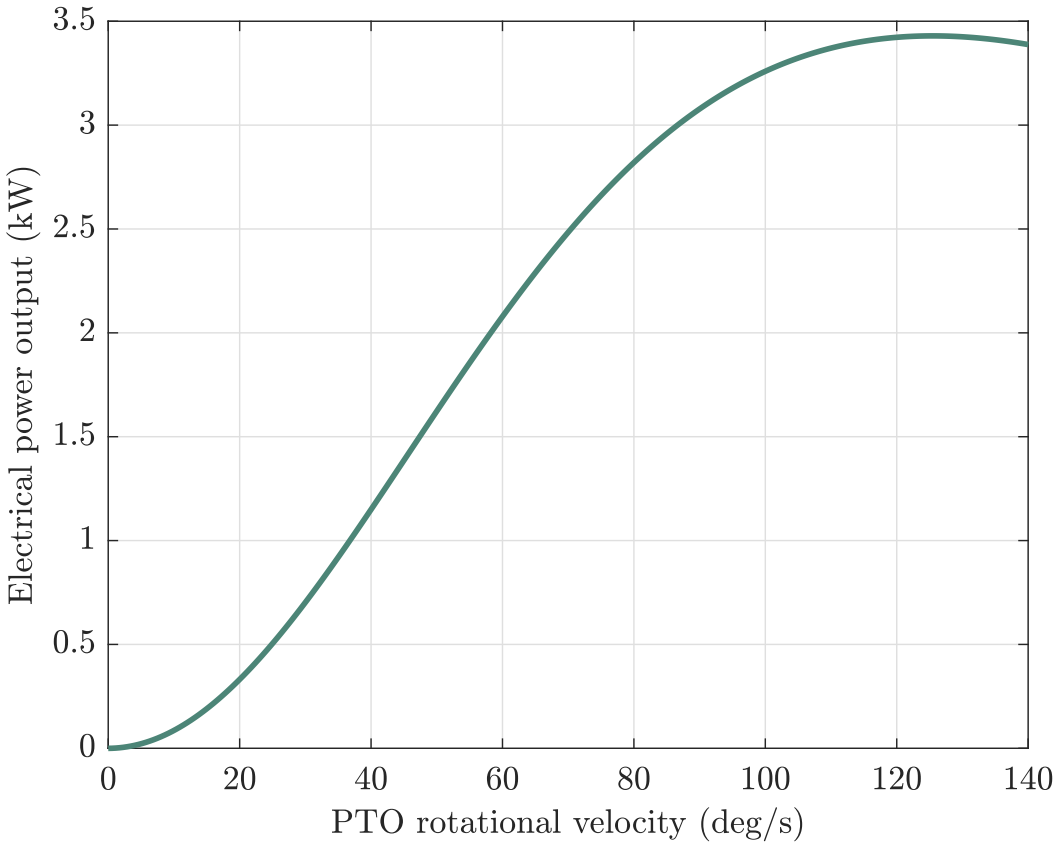

Figure A.2: Model of WEBS PTO used to estimate electrical power output from generator shaft speed.

Table A.1: System properties

Component	**Specification**
Nacelle diameter	0.5 m
Nacelle length	3 m
Nacelle mass	557 kg
Fore and aft float diameter	0.575 m
Fore and aft float length	3.1 m
Fore float mass	327 kg
Aft float mass	305 kg
PTO spring constant	668 Nm/rad
PTO damping coefficient	3092 Nms/rad
Spring reference angle	260°
Gearbox ratio	126.9
Gearbox efficiency	96%
Frictional torque	207 Nm
Heave plate mass	440 kg
Heave plate buoyancy	124 kg
Tether length	52.5 m
Tether stiffness	13.6 kN/m
Chain length	3 m
Chain mass	16.2 kg
Yoke Mass	159.8 kg

used to determine tether stiffness properties are based on manufacturer specifications (3/4" Samson Tenex). Additionally, the model used to estimate electrical power output for WEBS from PTO velocity ($\dot{\phi}$) is shown in Fig. A.2. This model was constructed using synchronized measurements of electrical power output and power take-off (PTO) velocity from WEBS field testing.

A.2 Dynamical model

The dynamical model (Proteus DS) relies on the parameters outlined in Appendix A.1. Floats and nacelle are constructed from standard cylinder rigid body features. The PTO is represented using a "RigidBodyConnectionABAJoint" with spring and damping coefficients

Table A.2: System properties for numerical simulation

Description	**Specification**
Nacelle I_{xx}	545.15 kg m^2
Nacelle I_{yy}	13.52 kg m^2
Nacelle I_{zz}	544.38 kg m^2
Nacelle center of gravity	[0 0 0] (relaxed state)
Fore float I_{xx}	559.2 kg m^2
Fore float I_{yy}	95.4 kg m^2
Fore float I_{zz}	640.3 kg m^2
Fore float center of gravity	[1.133 0 0] m
Fore arm cross section	0.229 x 0.0254 m
Fore arm length	1.09 m
Aft float I_{xx}	497.8 kg m^2
Aft float I_{yy}	73.7 kg m^2
Aft float I_{zz}	557.8 kg m^2
Aft float center of gravity	[-1.182 0 0] m
Aft arm cross section	0.229 x 0.0254 m
Aft arm length	1.01 m
Heave plate center of mass	[0 0 60.3] m
Generator/gearbox I_{yy}	18.9 kg m^2
Mooring yoke and mast I_{xx}	441 kg m^2
Mooring yoke and mast I_{yy}	118 kg m^2
Mooring yoke and mast I_{zz}	324.5 kg m^2
Mooring yoke center of gravity	[0 0.0948 -0.65] m

as specified in Table A.1. As Proteus DS may experience difficulties with hydrodynamics on concave surfaces, a solid cone is used to represent the heave plate, and buoyancy calculations within Proteus DS are turned off for the heave plate and specified manually.

The wave spectrum is defined using a Pierson-Moskowitz spectrum as described in [7]. This spectrum has a wave heading of 0°, period of 9.66 s, height of 1.33 m, with 270 wave segments and a wave seed of 12,345. The number of wave segments and peak period affect the return period of the wave field, or the length of time that a simulation is run before the wave field repeats. For this case, the maximum run time is 695 s. No wind or currents are included in this simulation.

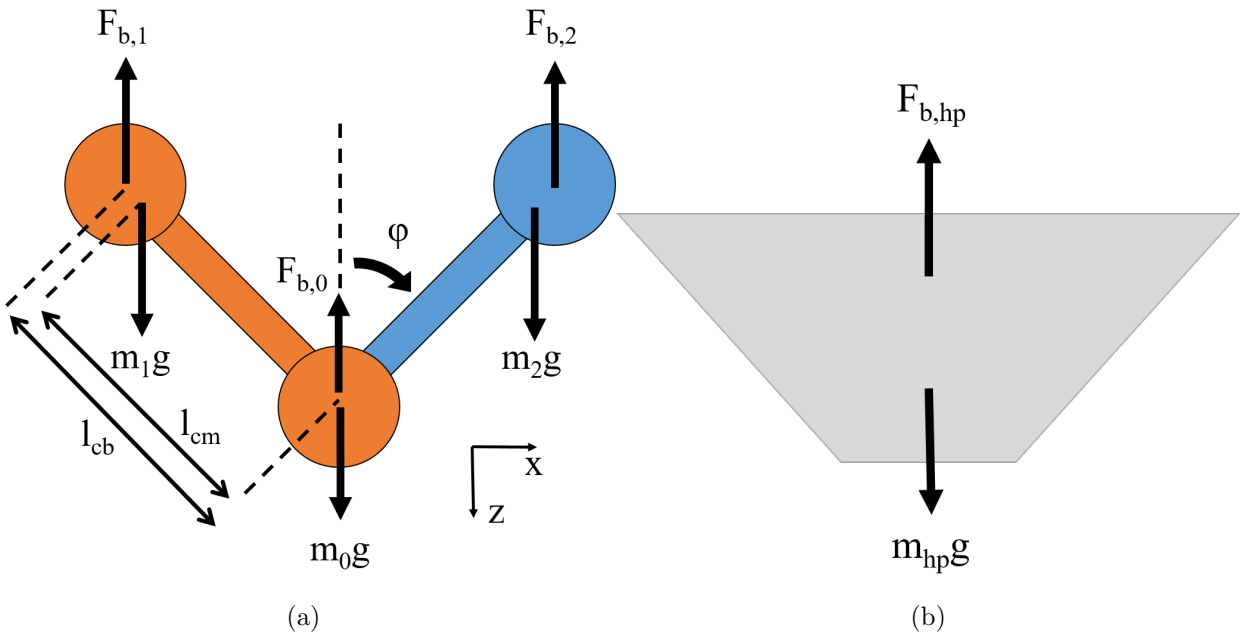

Figure A.3: Free body diagram for WEBS surface body and heave plate. l_{cb} denotes the distance from nacelle to center of buoyancy of the float, and l_{cm} denotes the distance from nacelle to the center of mass of the float.

A.3 Analytical model

The analytical model is constructed from the equations of linear motion governing the components of WEBS in the vertical direction and from the equations of rotational motion about the nacelle. From an initial set of equations describing the floats, nacelle, and heave plate, as well as compatibility conditions, these can be simplified to one equation in the vertical direction of motion and one equation to describe the rotation about the nacelle. A free body diagram describing the direction of force acting on the device in equilibrium is shown in Fig. A.3. The displacement between the center of mass and center of buoyancy (Fig. A.3a) affects the moments induced on the PTO by the forces of buoyancy and gravity, reflected in the equation of motion describing rotation about the nacelle:

$$\ddot{\phi}(J_{PTO} - J_1 - J_2) = \sin\phi[l_{cb}(F_{b,1} + F_{b,2}) - l_{cm}g(m_1 + m_2)] + 2k(\phi - \phi_0) - 2c\dot{\phi}. \tag{A.1}$$

In this equation, J_{PTO} is the rotational moment of inertia for the PTO, and J_1 and J_2 are the moments of inertia for the two floats about the nacelle. F_b represents forces of buoyancy on the nacelle (subscript 0), aft float (subscript 1), fore float (subscript 2), and heave plate (subscript hp). m represents mass, g is the gravitational constant, l_{cm} is the distance from the center of the nacelle to the center of mass of the float, l_{cb} is the distance to the center of buoyancy of the float, and *phi* is the angle of the arm from vertical. As ϕ is half of the angle between floats, $\phi_0 = 130°$. Finally, k is the spring constant and c is the damping constant used to approximate the PTO. The spring reference angle shown in Table A.1, represents the angle between floats at which the spring from the PTO exerts no force in the positive ϕ direction.

The equation of motion in the vertical (z) direction is:

$$\begin{aligned}(m_0 + m_1 + m_2 + m_{hp} + C_a\rho\pi/6D_{hp}^3)\ddot{z}_0 &= g(m_0 + m_1 + m_2 + m_{hp}) \\ &- [F_B + C_d(1/8\rho\pi D_{hp}^2)\dot{z}_0|\dot{z}_0|] \\ &- (m_0 + m_1)(l_{cm}\dot{\phi}^2\tan\phi\sin\phi + l_{cm}\dot{\phi}^2\cos\phi) \\ &- m_2(l_{cm}\dot{\phi}^2\tan\phi\sin\phi + l_{cm}\dot{\phi}^2\cos\phi).\end{aligned} \tag{A.2}$$

The added mass force of the heave plate is represented as a product of the coefficient of added mass C_a, the fluid density (ρ), the volume of a sphere with an effective diameter equal to that of the heave plate (D_{hp}), and the vertical acceleration of the plate ($\ddot{z}$). Buoyancy of all bodies is represented as $F_B = F_{b,0} + F_{b,1} + F_{b,2} + F_{b,hp}$. Drag is calculated as a product of the drag coefficient (C_d), the area of the heave plate, and the square of vertical velocity ($\dot{z}$). Because of the rigid coupling, heave plate motion is equal to nacelle motion.

In the model, these equations are solved for $\ddot{\phi}$ and $\ddot{z}$, respectively. We then rewrite the

equations as a set of first order linear ordinary differential equations, which we solve using ODE45 in MATLAB. The model updates every time step with new values for $F_{b,1}$ and $F_{b,2}$. These change based on the position of the floats with respect to mean water level ($z = 0$) at the current time step and the position of the free surface for the next time step. We assume the water surface is uniform and level across the floats.

These equations are derived from the full list of fundamental equations balancing rotational and linear forces, as well as compatibility conditions between the two sides of the system:

$$J_1\ddot{\phi} = (m_1 g - F_1)\sin\phi(l_{cm,1} g m_1 - l_{cb} F_{b,1}) + \tau_1 \tag{A.3}$$

$$(m_0 + m_1)\ddot{z}_{cm_1} = (m_0 + m_1)g + T_3 - (F_{b,0} + F_{b,1}) - T_{2z} \tag{A.4}$$

$$(m_0 + m_1)\ddot{x}_{cm_1} = T_{2x} \tag{A.5}$$

$$-J_2\ddot{\phi} = -\tau_2 + \sin\phi(F_{b,2} l_{cb} - m_2 g l_{cm,2}) \tag{A.6}$$

$$m_2\ddot{z}_{cm_2} = m_2 g - F_{b,2} + T_{2z} \tag{A.7}$$

$$m_2\ddot{x}_{cm_2} = -T_{2x} \tag{A.8}$$

$$\ddot{x}_{cm_1} = \ddot{x}_0 - l_{cm,1}\ddot{\phi}\cos\phi + l_{cm,1}\dot{\phi}^2\sin\phi \tag{A.9}$$

$$\ddot{z}_{cm_1} = \ddot{z}_0 + l_{cm,1}\ddot{\phi}\sin\phi + l_{cm,1}\dot{\phi}^2\cos\phi \tag{A.10}$$

$$T_3 + F_{hp} - m_{hp} g = -m_{hp}\ddot{z}_{hp} \tag{A.11}$$

$$\ddot{x}_{cm_2} = \ddot{x}_0 + l_{cm,2}\ddot{\phi}\cos\phi - r_{cm,2}\dot{\phi}^2\sin\phi \tag{A.12}$$

$$\ddot{z}_{cm_2} = \ddot{z}_0 + l_{cm,2}\ddot{\phi}\sin\phi + l_{cm,2}\dot{\phi}^2\cos\phi \tag{A.13}$$

$$J_{PTO}(\ddot{\phi}) = \tau_1 + \tau_2 + 2k(\phi - \phi_0) - 2c\dot{\phi} \tag{A.14}$$

$$F_{b,1} = \rho g l_f \left[\pi R_1^2 - R_1^2\cos^{-1}\left(\frac{\eta(t) - z_1(t)}{R_1}\right) ... \right.$$
$$\left. + (\eta(t) - z_1(t))\sqrt{R_1^2 - (\eta(t) - z_1(t))^2}\right] \tag{A.15}$$

$$z_1 = z_0 - l_{cb}\cos\phi \tag{A.16}$$

$$F_{hp} = C_d\left[\frac{1}{8}\rho\pi D_{hp}^2\right]\dot{z}_{hp}|\dot{z}_{hp}| + C_a\rho\frac{\pi}{6}D_{hp}^3\ddot{z}_{hp} + F_{b,hp} \tag{A.17}$$

Appendix B

EFFECT OF GEOMETRY ON HEAVE PLATE HYDRODYNAMICS

The following section covers additional results from experiments on heave plate geometry that were presented at the Marine Energy Technology Symposium in 2018. This study was conducted in collaboration with CalWave (Berkeley, CA, U.S.)

B.1 Methods

This study assesses the hydrodynamic forces generated by thirteen different heave plates, all shown in Figure B.1. Three geometric groups are tested: squares, rectangles, and so-called "Newman shapes". These groups contain two heave plate types: solid and perforated. The area enclosed by the perimeter of each heave plate is identical (0.16 m^2). The perforated plates have a constant solidity of 90%, but varied hole sizes. Of the five square plates, one is solid and the remaining four have 2, 4, 6, and 10 holes, as shown in Figure B.1. Five rectangular plates, with a 2:1 aspect ratio, are also tested, with 0, 4, 6, 8, and 10 holes. The Newman shapes, whose geometries are based on a weighted sum of sines and cosines, are inspired by work to amplify surface waves conducted by J. N. Newman [20]. The last row of Figure B.1 shows the three Newman shapes, which we denote A, B, and C, from left to right. These shapes allow for large changes in perimeter while maintaining constant projected area.

The heave plates are tested using the vertically oriented linear actuator placed at the edge of a dock as described in Chapter 2. Total force induced in the heave direction is measured using a 2200 N rated S-beam load cell, with a noise floor of about 3 N, and the data acquisition system records force and position at 2 kHz. The water at the side of the dock is open to recreational boating and small commercial shipping traffic, but the occasional

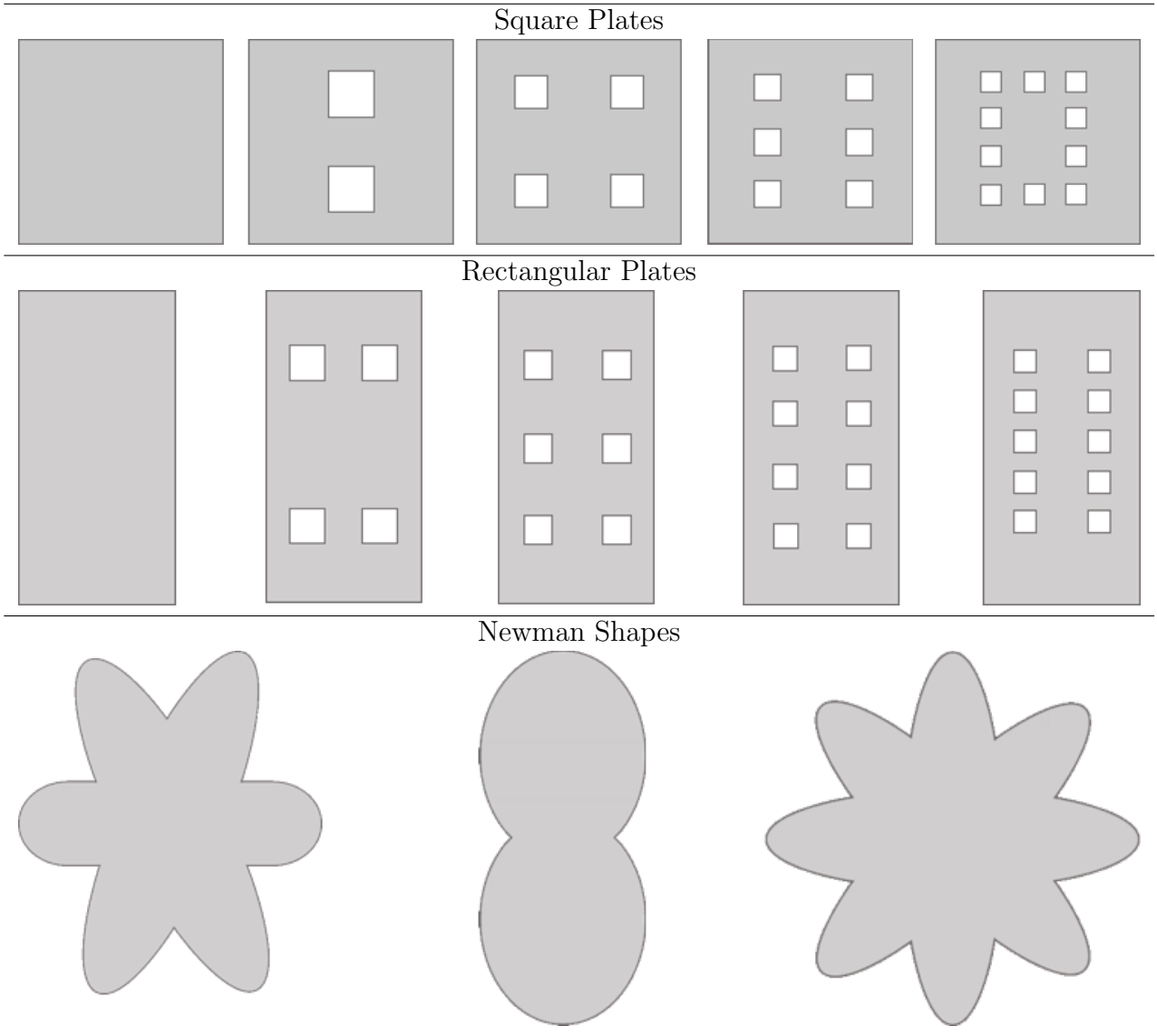

Figure B.1: Heave plates used in varied geometry testing

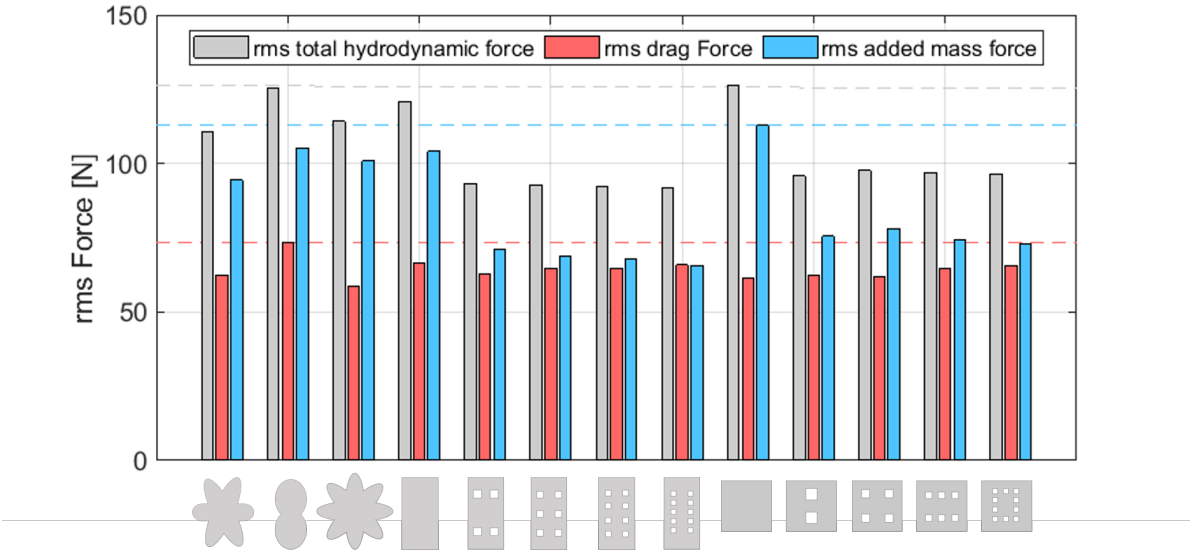

Figure B.2: Plot of rms total hydrodynamic force (based on the force reconstruction) for each plate, alongside the rms drag and added mass forces, when $KC = 0.35$ and $T = 0.5$ s.

wakes that reach the dock are of minimal size, and are observed to have negligible impact on the data. The distance from water surface to mean plate position is 1.02 m, with a total water depth of just over 3 meters and effectively unbounded sides. Both surfaces are more than two diameters away from mean plate position, indicating negligible surface effects [9].

The suite of tests is the same for each plate, covering periods from 0.5 - 4 s, and KC numbers from 0.14 - 5.59. Critical to this analysis, in Eq. 1.5, we use an effective diameter, D, defined as the diameter of a circle with area equal to that of the test plate. This definition results in an equal effective diameter for all heave plates tested.

Sinusoids producing higher forces (larger amplitude and higher frequency) improve the signal to noise ratio, but are limited by the maximum Oscillator speed of about 0.65 m/s. Table B.1 shows the maximum speeds reached for each test. As the KC number increases, a larger oscillation period is required due to the maximum speed restriction. For each new period, an overlap in KC number with other periods allows for analysis of frequency dependence.

Table B.1: Maximum cycle speed (cm/s) for each conducted test.

	Period (s)			
KC	0.5	1.0	2.0	4.0
0.14	12.6			
0.21	18.8			
0.28	25.1	12.6		
0.35	31.4	15.7		
0.52	47.1	23.6		
0.7		31.4	15.7	
1.4		62.8	31.4	
2.09			47.1	
2.79			62.8	31.4
4.19				47.1
5.59				62.8

These heave plates are candidates for field-testing with a small wave energy converter deployed in a scaled wave environment, with expected heave plate KC ¡ 1. Therefore, as seen in Table B.1, experimental assessment focuses on KC numbers in this range, with a more limited set of experiments to explore hydrodynamic responses to larger oscillation amplitudes.

Data analysis follows the methods outlined in Chapter 2.

B.2 Results and Discussion

Figure B.2 provides a summary of the balance of forces acting on the thirteen plates tested for a single KC number and period. We note that the rms hydrodynamic force is not equal to the sum of drag and added mass forces because those two forces are out of phase.

As shown in Figure B.2, the solid square plate produced the largest total hydrodynamic force, as well as the largest added mass force. Additionally, the forces decrease dramatically when holes are added, in line with prior results [13, 5, 32], with little change as the number

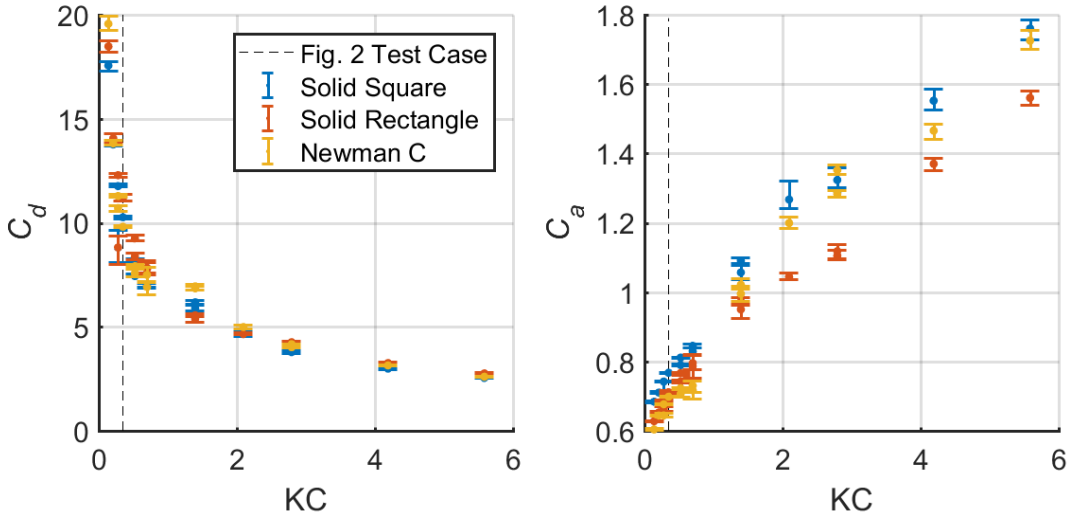

Figure B.3: Calculated coefficients of drag and added mass for the tests with the solid square (blue), the solid rectangle (red), and Newman plate C (yellow). The error bars represent the 25th and 75th percentile, with respect to the median value, and the dashed line shows the case depicted in Figure B.2.

of holes increases (porosity held constant). Newman shape B has a force breakdown that is similar to the solid rectangle, likely due to the similarity in shape between the two. Figure B.2 emphasizes the dominance of added mass forces at low KC number in solid plates, and displays how the added mass and drag forces are nearly equivalent for plates with holes.

Trends in the hydrodynamics for all tests are shown in Figure B.3. Coefficients of drag and added mass are dependent on the KC number, and independent of oscillation frequency. The coefficient of drag is highly nonlinear for KC ¡ 1, and asymptotes to a constant value at higher KC numbers. In contrast, the coefficients of added mass follow a linear, increasing trend across the range of KC numbers tested.

Comparisons between the three plate groups are also instructive. Figure B.3 shows that at high KC numbers, drag coefficients are nearly invariant across the geometries, with only slight differences at small KC numbers. At low KC numbers, the square plate has the highest added mass coefficient, while the Newman plate the smallest. For KC ¿ 1, the

Newman plate overtakes the rectangle, and even approaches the added mass of the square. This suggest that, at low KC number, the added mass may be governed by some cross-plate length scale. For smaller cross-plate distances, plates may exhibit lower added mass coefficients, while larger distances would result in higher coefficients. This makes continuous, symmetric shapes (such as the square) more desirable for wave energy conversion. For high KC numbers, small features, such as the concave corners of Newman shape C, may become engulfed in the boundary layer of the plate, changing the effective cross-plate distance. This leads to strikingly similar hydrodynamics between different radially symmetric shapes at high KC numbers, despite their differences at low KC number.

Not shown in the plots, radially symmetric plates tend to exhibit greater stability in the surge and sway directions than asymmetric plates. For example, on some oscillations, the rectangular plates induce a slight side-to-side vibration, a phenomenon not seen in the squares. Additionally, Newman plates A and B, which are less radially symmetric, experience similar vibration, while the more radially symmetric plate C is more stable.

B.3 Conclusions

At low KC numbers, added mass is the dominant component of the total hydrodynamic force, but is significantly reduced when porosity is introduced. Drag shows little change between all of the plates tested.